7-16-2014

Studies of Electronic Inhomogeneities in Strongly Correlated Systems Using Quantum Cluster Methods

Kun Fang
Univerisity of Connecticut, Storrs, kun.fang@uconn.edu

Studies of Electronic Inhomogeneities in Strongly Correlated Systems Using Quantum Cluster Methods

Kun Fang, Ph.D.

University of Connecticut, 2014

In order to understand various local phenomena related to electronic phase separation discovered recently in strongly correlated materials, quantum cluster methods are applied to a theoretical model, *i.e.*, Hubbard model, which has successfully predicted basic properties of strongly correlated systems. Our calculations are performed at two levels: exact calculations based on the isolated small clusters via exact diagonalization and approximate calculations applied to large lattices using the variational cluster approximation (VCA).

We first study phase separation instabilities with the formation of a pairing gap in the two-dimensional Hubbard model for 8-site Betts clusters. The exact diagonalization method is applied to extract exact ground and excited states of the Hubbard model. The results show that the electronic states with one hole off

half filling are unstable and they energetically prefer creating the spatial phase separation. The effect of next nearest hopping is also discussed in this part.

We studied the variation of the pairing when the out-of-plane correlation is present by adding an interacting apical site above the two-dimensional cluster plane. The calculations indicate that the out-of-plane correlation can be detrimental to the in-plane pairing effect. When it is not too strong to destroy electron pairs on the plane, the modulation of the apical site can drive the pairing gap to show a sinusoidal variation which is consistent with recent experimental discoveries.

Variational cluster approximation is introduced to explore local properties of larger lattices. The local nematic state is studied in the square lattice using this method, which indicates that it is possible that the electronic states can locally break the C_4 symmetry (90° rotational symmetry) to form a pattern where the electronic properties, such as charge and spin correlations, are different in x and y directions. The spatial phase separation in the square and honeycomb lattices is also investigated by the variational cluster approximation. The study shows that Coulomb interaction and lattice geometry are both crucial for electronic phase separation. We propose that electronic phase separation is the result of an instability of the Fermi surface at the boundary of the first Brillouin zone of antiferromagnetic states.

Studies of Electronic Inhomogeneities in Strongly Correlated Systems Using Quantum Cluster Methods

Kun Fang

B.S., University of Science and Technology of China, Hefei, China 2007

A Dissertation

Submitted in Partial Fullfilment of the

Requirements for the Degree of

Doctor of Philosophy

at the

University of Connecticut

2014

APPROVAL PAGE

Doctor of Philosophy Dissertation

Studies of Electronic Inhomogeneities in Strongly Correlated Systems Using Quantum Cluster Methods

Presented by

Kun Fang,

Major Advisor

Gayanath Fernando

Associate Advisor

Joseph Budnick

Associate Advisor

Boris Sinkovic

University of Connecticut

2014

I would like to dedicate my thesis to my parents for their affection, love and encouragement.

ACKNOWLEDGEMENTS

I would like to express my deep and sincere gratitude to my advisor, Prof. Gayanath Fernando. His wide knowledge and scientific perspective had been of great value for me. His understanding, encouraging and guidance throughout these years led me into an amazing world of strongly correlated system. Without his financial and academic supports, I could not go through the most difficult time in my PhD life.

I am deeply grateful to our collaborator, Prof. Armen Kocharian at the California State University, Los Angeles. He contributed great suggestions to my research work. Discussion with him was always enjoyful and valuable. His connections with many great guys in this field also provided another kind of support to my research.

I wish to express my warm and sincere thanks to Prof. Joseph Budnick and Prof. Boris Sinkovic, who are my associate advisors, and Prof. Barrett Wells. Although they did not participate in my research work directly, their comments on my work and discussions with them helped me understand concerns from experiments and other fields, which were important inspirations to me.

This thesis includes results of researches carried out in Physics Department at the University of Connecticut using computing facilities at the Center for Integrated

Nanotechnologies in Los Alamos National Laboratory and the Center for Functional Nanomaterials in Brookhaven National Laboratory. Many people in these institute had offered helps to my researches. I would like to thank all of them.

Aside from my researches, my life had been enriched by a lot of interesting friends I met at the University of Connecticut. I would like to thank them for making my stay in Connecticut a pleasant experience.

Finally, I owe my warmest love and eternal thanks to my parents, for their unconditional affection and support; to my fiancee Yun, for her love and companionship throughout these years.

TABLE OF CONTENTS

LIST OF FIGURES

Chapter 1

Introduction

1.1 Strongly correlated systems

In condensed matter physics, we already have a clear understanding of regular metals, insulators and semiconductors from single-particle band theory [1]. The ground state properties of these materials can be quantitatively obtained by density functional theory [2]. The low-energy excitations in these system are well described by Landau Fermi liquid theory [3]. Perturbation theory [3] is also successfully applied in these materials with dopants. In the past few decades, the field of the strongly correlated electron systems has gained theoretical and experimental significance since the discovery of the high temperature superconductors. They are a family of chemical compounds based on transition and rare-earth elements with partially filled or empty $3d$, $4f$ or $5f$ orbitals. Because of the strong Coulomb interaction due to d and f electrons, a broad range of anomalous behaviors are observed in these strongly correlated materials, such as metal-insulator

transitions, Kondo effect, various magnetic states, high temperature superconductivity, inhomogeneity and so on [4], which lead to complex phase diagrams. The Fig. 1.1 shows a typical phase diagram of the high temperature superconductors (HTSCs), which contains many different phases. In strongly correlated materials, the strength of the Coulomb interaction is larger or comparable to the band width of $3d$, $4f$ and $5f$ electrons, so a traditional perturbation treatment fails to adequately address the electronic structure and related properties. Although intensive research efforts have been devoted during the past decades and many new concepts have been proposed for the complex phenomena found in various experiments, we are still far from a comprehensive understanding of some basic properties of this material such as pairing mechanism, linear resistivity and pseudogap phase in HTSCs.

The theoretical investigation of the strongly correlated materials began from exploring the metal-insulator transition and various magnetic phenomena. After the discovery of high temperature superconductivity in the cuprate materials, many physicists believe that a suitable model for these materials is the Hubbard Model [6]. In recent decades, more and more abstract models have been proposed to solve different problems, for example, the Hubbard model, the Kondo lattice model [7], the Periodic Anderson model [8] and so on. Although these models describe systems which are apparently a lot simpler than the complex atomic structures related to this class of materials, they, in particular the Hubbard model,

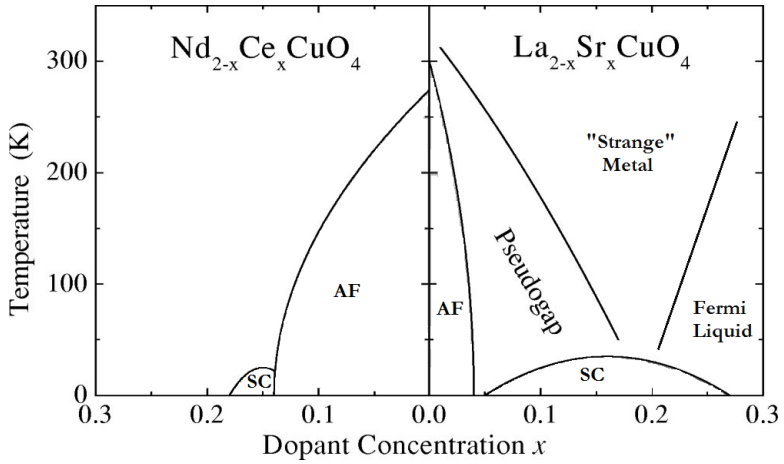

Fig. 1.1: A schematic phase diagram of HTSC for hole doping (right side) and electron doping (left side) from Ref. [5]

are of enormous intrinsic interest and known to yield results that are consistent with various experiments. In spite of the success of various models and intensive worldwide research efforts in recent decades, there is still no consensus among the scientists on many important topics such as pairing mechanism for High T_c superconductivity and the formation of various complex phases. At the same time, more and more unexpected phenomena are observed with the invention of more sophisticated experimental tools and these new phenomena provide more clues towards a better understanding of these interesting materials.

1.2 Electronic inhomogeneities

Recent advances in experimental physics, especially the invention of state-of-the-art scanning Scanning Tunneling Spectroscopy (STS), have clearly shown the

existence of a new phenomenon: electronic inhomogeneities in cuprates [9–11], iron-based superconducting materials [12] and even heavy fermion materials [13]. These microscopic inhomogeneities, sometimes called microscopic phase separation (PS) in some cases, are present as spatial variations of the material properties (for example, gap sizes and hole concentrations) at multiple length scales in the form of stripes [14], "checkerboard" [15], granular structures [16] and other forms [17], even if the crystal lattice is perfectly homogenous [18]. These cited references are just a few part of a great number of works that discovered this phenomenon in various strongly correlated materials, so it seems the electronic inhomogeneity is an intrinsic property in strongly correlated system (shown in Fig. 1.2).

The importance of electronic inhomogeneities driven by electron correlations was realized in the Hubbard model by Visscher [20] in 1970s and systematically studied later in Ref. [21] which predicted an intrinsic tendency toward phase separation at strong interaction limit using the $t - J$ model. The physics behind phase separation is that when the half-filled antiferromagnetic insulator is doped with holes, compared to a uniform distribution of electrons, the energy of the system decreases, if the holes get together to generate variations of hole rich and hole poor regions. Thus, phase separation forces holes to concentrate into a small region. The phenomenon resembles an effective attraction among the holes although the microscopic interactions between them are repulsive. They further proposed that phase separation might give rise to high temperature supercon-

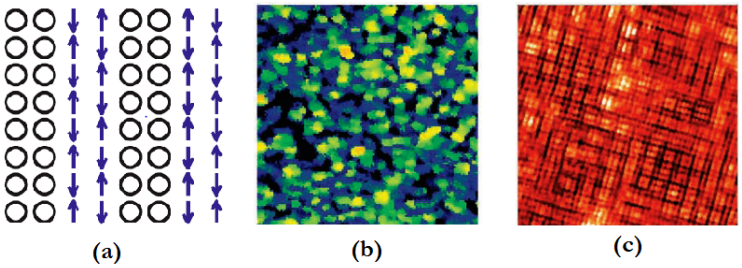

Fig. 1.2: Some examples of electronic inhomogeneities in strongly correlated system: (a) A schematic diagram of the stripe phase from Ref. [19]. (b) Inhomogeneous gap distribution from STM measurement on a $56nm \times 56nm$ $BSCCO$ sample from Ref. [16]. (c) The STM measurement shows the "checkerboard" pattern on a $16nm \times 16nm$ $Ca_{2-x}Na_xCuO_2Cl_2$ sample with checkerboard-like modulation periodicity equal to 4 times the lattice constant.

ductivity (HTSC) [22]. Su [23] reported the absence of phase separation in the one-band Hubbard model on a square lattice. He introduced a pseudo-spin field based on the symmetry of the Hubbard model to solve the Hubbard model, which was similar to a mean field, so the approach was not able to catch important local effects. Our group later extended exact calculations on phase separation to the Hubbard model based on several different bipartite clusters [24–28] using exact calculations. The results proposed for small clusters show similar phase separation from small to moderate Coulomb interactions at larger doping levels even around the optimal doping, but the cluster calculations always are invariably tied to some uncertainties due to size and edge effects. Macridin et al. [29,30] proposed a thermodynamical description of electronic phase transition, and the theory further points to the existence of a quantum critical point. Aichhorn et al. [31,32] discussed the coexistence of the global antiferromagnetic and superconducting orders by introducing two Weiss fields parameters in their VCA calculation, but the results does not support any microscopic local phase separations since the long-range orders are applied. Recently, Sboychakov et. al. [33,34] investigated the electronic phase separation which is caused by imperfect nesting of the Fermi surface in AA-stacked bilayer graphene and iron pnictides. They shows a different mechanism of the electronic phase separation which is not directly related to electron correlations.

1.3 Hubbard Model

As mentioned in the previous sections, quantum mechanical studies of strongly correlated electronic systems are usually based on several idealized models. Among them, the most simplified model is the one-band Hubbard model and its derivatives. The Hubbard model only accounts for the motion of electrons in the lattice and short-range Coulomb repulsion. In spite of the simplicity of Hubbard model, it is believed that the model exhibits ample interesting phenomena found in various observed phenomena such as the metal-insulator transition, antiferromagnetism, ferromagnetism, superconductivity and so on.

The Hamiltonian of the Hubbard model H is usually written as the sum of a non-interacting part H_0 and an interacting part H_I:

$$H = H_0 + H_I$$

H_0 represents quantum mechanical hopping of electrons between lattice sites. The hopping of electrons near the fermi surface can be well described by the tight binding approximation. The general form of this term is

$$H_0 = \sum_{\boldsymbol{r},\boldsymbol{r}'} \sum_{\sigma} t_{\boldsymbol{r},\boldsymbol{r}'} c^{+}_{\boldsymbol{r}\sigma} c_{\boldsymbol{r}'\sigma} \tag{1.1}$$

where $\boldsymbol{r}$ denotes a lattice vector and $c_{\boldsymbol{r}\sigma}$ ($c^{+}_{\boldsymbol{r}\sigma}$) is the annihilation (creation) operator of electrons at lattice site $\boldsymbol{r}$ with spin index σ. $t_{\boldsymbol{r},\boldsymbol{r}'}$ is the hopping parameter between lattice sites $\boldsymbol{r}$ and $\boldsymbol{r}'$, which is proportional to the probability of one

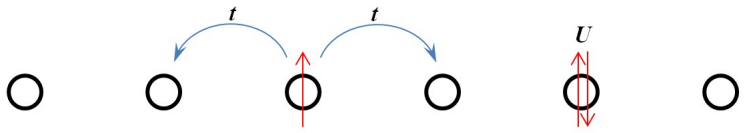

Fig. 1.3: A schematic representation of the one-dimensional Habbard model.

electron jumping from lattice site $\boldsymbol{r}$ to $\boldsymbol{r}'$. The strong interaction among electrons caused by localized characters of d or f orbitals on the same lattice site is represented by the interacting term H_I:

$$H_I = \sum_{\boldsymbol{r}} U_{\boldsymbol{r}} n^+_{\boldsymbol{r}\uparrow} n_{\boldsymbol{r}\downarrow} = \sum_{\boldsymbol{r}} U_{\boldsymbol{r}} c^+_{\boldsymbol{r}\uparrow} c_{\boldsymbol{r}\uparrow} c^+_{\boldsymbol{r}\downarrow} c_{\boldsymbol{r}\downarrow} \tag{1.2}$$

where $U_{\boldsymbol{r}}$ is the screened Coulomb interaction at the lattice site $\boldsymbol{r}$, which is usually a constant. This term introduces an energy cost $U_{\boldsymbol{r}}$ when two electrons with different spins occupy the same orbital state at the same lattice site $\boldsymbol{r}$. Although the original Coulomb interaction is long-ranged, the Hubbard model only takes the on-site interaction into account which is the strongest part. Fig. 1.3 is a schematic example of hoppings and interactions in the Habbard model in one dimension. The system gains an energy t when an electron hops to a neighboring site while two electrons with opposite spins can stay in the same site with an energy cost U.

Rigorous theoretical treatments of the Hubbard model are limited to the 1-dimensional case based on the Bethe ansatz [35]. Theorists found themselves facing extreme difficulties in two or more dimensions, since the Bethe ansatz is

not applicable for more than one dimension. There are basically two approaches to solve the Hubbard model in two or higher dimensions. One can apply exact numerical calculations on a Hubbard model with limited size, *i.e.* a Hubbard cluster. This method involves exactly diagonalizing the Hamiltonian, so it is usually called exact diagonalization (ED). The details of this method are introduced in Sec. 2.1. The method can solve the Hamiltonian for all or several low lying eigenstates and their energies. The ground-state properties and thermodynamical properties of the model are extracted from the information of eigenstates. The other method uses an analytical or numerical method based on some approximations to get a solution for the infinite lattice. This method mostly focuses on calculating the green's function, which can equivalently provide various information of the ground state of the system. The most important approximation is based on mean field theory (MFT), which replaces all the many-body interactions by an effective (mean) external field, so it reduces the model into an single particle problem. Because of averaging all the interactions, MFT fails to capture some local physical effects because it ignores the spatial and temporal fluctuations [36]. The popular dynamical mean field theory (DMFT) resolves the temporal fluctuations (for a review see Ref. [37]) but still suffers from the critical flaw of neglecting spatial fluctuations. In order to solve the problem, many efforts have been made to add local correlations to the mean field theories. Some successful attempts are obtained by extending mean field theory to a quantum cluster extension, such as

cluster perturbation theory (CPT) [38], cellular DMFT (C-DMFT) [39], dynamical cluster approach (DCA) [40], variational cluster approximation (VCA) [41], etc.

In this thesis, we use both ED and VCA methods to study electronic inhomogeneities in the Hubbard model based on several different lattices. In Chapter 2, the ED and VCA methods are introduced. For ED method, the Lanczos method which can calculate several lowest lying eigenstates is discussed. The VCA method is derived from some basic many-body theories and its developments and applications are discussed in detail. The basic idea of electronic inhomogeneities within the quantum cluster theory is introduced in Chapter 3. The ED method is used in this chapter to create a physical insight of electronic PS based on results of isolated clusters. In Chapter 4, the same logic based on calculation of isolated clusters is applied explain a specific inhomogeneous phenomenon: gap modulations, which involve out-of-plane effects in cuprates. Since calculations based on isolated clusters always suffer from the limited cluster size and edge effects, the VCA method is developed for the future studies. In Chapter 5, the VCA method is employed for a study of the local nematic order in the Hubbard model based on a square lattice. In Chapter 6, a further research of electronic inhomogeneities is perform based on the VCA calculations. The calculations extend to the honeycomb lattice which is shown absence of the electronic inhomogeneity. Based on the comparison between the square lattice and honeycomb lattice, the possible

mechanism of electronic inhomogeneities is proposed.

Chapter 2

Methodology

2.1 Exact Diagonalization (ED)

The simplest and exact solution of the Hubbard model comes from exact diagonalization (when it is possible). The idea is to project the Hamiltonian H to a certain set of basis $|\psi\rangle$, so that the Hamiltonian can be written as a matrix with matrix elements $H_{i,j}$ determined by $\langle\psi_i|H|\psi_j\rangle$. The Hamiltonian matrix is then solved exactly to get eigenvalues and eigenvectors by either a full diagonalization method [42] (for the full spectra) or lanczos method [43] (for several low lying states). The ED method can provide very high numerical accuracy for at lease part of the spectra, but since the ED algorithm requires a large amount of memory and time, the ED method is strongly restricted by the size of the system. Right now, the largest size in most ED study of Hubbard model is only 4×4, which is too small to compare to any real material used in experiments. Therefore, although

the ED method can provide accurate results, these results suffer from finite size effects and edge effects. Many other approximate methods have been introduced in order to treat large lattices while trying to keep the results relatively accurate.

2.1.1 Lanczos method

In most studies of strongly correlated systems, only several low-lying states are mostly relevant to problems in strongly correlated systems since most experiments are performed at low temperatures at which only some low-energy excitations are allowed. Therefore, a full diagonalization is not really necessary for most of studies and Lanczos method is usually used to extract the ground state and several low energy excitation states of the system.

The basic idea of the Lanczos method is to project the Hamiltonian H onto a subspace which is called Krylov subspace $\mathscr{K}$, which is spanned by repeatedly applying the Hamiltonian H to an arbitrary vector $|\phi_0\rangle$:

$$\mathscr{K}_r \equiv span\{|\phi_0\rangle, H|\phi_0\rangle, H^2|\phi_0\rangle, \ldots, H^{r-2}|\phi_0\rangle, H^{r-1}|\phi_0\rangle\} \tag{2.1}$$

The Hamiltonian H can be rewritten as new matrix in the Krylov subspace. Since the generating vectors in Eq.2.1 are not mutually orthogonal, the new matrix is built upon a set of orthonormal vectors of the Krylov subspace $|\phi_i\rangle$ $(i = 0, \ldots, r)$. The orthogonal vectors are constructed following the recursive relation:

$$\begin{aligned} |\phi_1\rangle &= H|\phi_0\rangle - \frac{\langle\phi_0|H|\phi_0\rangle}{\langle\phi_0|\phi_0\rangle}|\phi_0\rangle \\ |\phi_{i+1}\rangle &= H|\phi_i\rangle - a_i|\phi_i\rangle - b_i^2|\phi_{i-1}\rangle, \quad i = 1, \ldots, r \end{aligned} \tag{2.2}$$

where

$$a_i = \frac{\langle \phi_i | H | \phi_i \rangle}{\langle \phi_i | \phi_i \rangle}, \quad b_i^2 = \frac{\langle \phi_i | \phi_i \rangle}{\langle \phi_{i-1} | \phi_{i-1} \rangle}, \tag{2.3}$$

and the orthonormal vectors are found by $|i\rangle = |\phi_i\rangle / \sqrt{\langle \phi_i | \phi_i \rangle}$. It is easy to see that the projection of H on the Krylov subspace is a tridiagonal matrix with the following form:

$$H = \begin{pmatrix} a_0 & b_1 & 0 & 0 & \dots & 0 & 0 \\ b_1 & a_1 & b_2 & 0 & \dots & 0 & 0 \\ 0 & b_2 & a_2 & b_3 & \dots & 0 & 0 \\ \vdots & \vdots & \vdots & \vdots & \ddots & \vdots & \vdots \\ 0 & 0 & 0 & 0 & \dots & a_{r-1} & b_r \\ 0 & 0 & 0 & 0 & \dots & b_r & a_r \end{pmatrix} \tag{2.4}$$

The tridiagonal matrix can be easily diagonalized by some fast algorithm designed for tridiagonal matrices (see Chapter 11 in Ref. [42]) and the eigenvalues of the new matrix are also the eigenvalues of the original Hamiltonian. The eigenvectors of the original system are found by an inverse projection of the eigenvectors of the tridiagonal matrix in Eq.2.4 from Krylov subspace back to the original space. The number of low lying eigenvalues that can converge in the method is determined by the number of dimensions of Krylov subspace (r). Typically, the ground state of the system can be found by using a subspace with a very small number of dimensions (usually $r \sim 100$).

The basic Lanczos method is very helpful in finding eigenvalues of the o-

riginal Hamiltonian, but it cannot tell whether there is any degeneracy in the obtained eigenvalues. In theory, one can choose a new random vector $|\phi_0\rangle$ which is orthogonal to all known eigenvectors and this will result in new eigenvectors for the degenerate eigenvalues, so the degeneracy of all the eigenvalues can be found by iteratively using new random vectors $|\phi_0\rangle$ until no new eigenvectors can be found. However, the practical calculations performed in computer always have by round-up errors. The process to find a vector orthogonal to all known vectors can be ruined quickly by round-up errors, which makes finding degeneracies very difficult if a lot of low lying states are involved. In order to get around this difficulty a method called block Lanczos method is employed, which still use the same idea of the basic Lanczos method, but the Krylov subspace in block Lanczos method is not spanned by one but L orthogonal random vectors (All the required eigenvectors are calculated at the same time with only one or two iterations, so round-up errors are not large enough to break the orthonormal process here):

$$\begin{aligned} \mathscr{K}_{Lr} \equiv\ & span\{|\phi_1\rangle, \ldots, |\phi_L\rangle, H|\phi_0\rangle, \ldots, H|\phi_L\rangle, \ldots, \\ & H^{r-1}|\phi_0\rangle, \ldots, H^{r-1}|\phi_0\rangle\} \end{aligned} \tag{2.5}$$

The same orthonormal rule is used to create the basis of the Krylov subspace and a new Hamiltonian matrix is constructed. The new matrix is no longer a tridiagonal matrix but a *block* tridiagonal matrix. The method can provide all the eigenvectors of degenerate eigenvalues within only one Lanczos iteration, so it avoids possible problems caused by round-up errors in the iterative calculation.

2.2 Variational Cluster Approximation (VCA)

The time and memory requirements of exact cluster calculations increase exponentially as the number of site in the cluster, so it is impossible to calculation a cluster that is large enough to compare to the size of a real lattice used in any experiments. In order to study the Hubbard model on a large lattice, several approximate methods have been developed. We use Variational cluster approximation (VCA) in our studies.

2.2.1 Self-energy Functional Approach (SFA)

The VCA method is the quantum cluster extension of self-energy functional approach (SFA), so it is necessary to introduce SFA first. The goal of SFA is to provide an analytical method to find out the ground state of an interacting fermionic system. The theory is based on the concept of Luttinger Ward (LW) functional.

Luttinger-Ward functional

The LW functional provides an alternative way to solve interacting fermionic problem instead of perturbation theory. We consider a fermionic system described by Hamiltonian H, which includes non-interacting and interacting parts. In the

grand canonical ensemble, the partition function can be written as

$$Z = \int \mathcal{D}[\psi^*, \psi] \exp\{-\mathcal{S}[\psi^*, \psi]\} \tag{2.6}$$

where ψ^* and ψ are two Grassman fields and $\mathcal{S}$ is the action of the system:

$$\mathcal{S} = \int_0^\beta d\tau \{\sum_\alpha \psi^*_\alpha(\tau)(\frac{\partial}{\partial\tau} - \mu)\psi_\alpha(\tau) + H(\psi^*_\alpha(\tau+), \psi_\alpha(\tau))\} \tag{2.7}$$

We can introduce a bilinear source J coupled with field operators $\psi^*\psi$, so the partition function is defined as a functional of J

$$\mathcal{Z}[\boldsymbol{J}] = \int \mathcal{D}[\psi^*, \psi] e^{-\mathcal{S}[\psi^*,\psi] + \int_0^\beta d\tau d\tau' \sum_{\alpha,\alpha'} \psi^*_\alpha(\tau) J_{\alpha,\alpha'}(\tau,\tau') \psi'_\alpha(\tau')} \tag{2.8}$$

The one particle green's function can be obtained as the functional derivative of the grand potential energy, which is derived from $\ln \mathcal{Z}[J]$

$$\mathcal{G}(\alpha, \tau, \alpha'\tau') = -\frac{\partial \ln \mathcal{Z}[J]}{\partial J_{\alpha,\alpha'}(\tau, \tau')} \tag{2.9}$$

In a non-interacting system, *i.e.*, $H_i = 0$, the Hamiltonian can be writen as $H = H_0 = \sum_\alpha \psi^*_\alpha(\tau) H_0 \psi_\alpha(\tau')$, so the partition functional can be simplified:

$$\begin{aligned} \mathcal{Z}[\boldsymbol{J}] &= \int \mathcal{D}[\psi^*, \psi] e^{-\int_0^\beta d\tau d\tau' \sum_{\alpha,\alpha'} \psi^*_\alpha(\tau)((\frac{\partial}{\partial\tau} - \mu + H_0)\delta(\tau-\tau') - J_{\alpha,\alpha'}(\tau,\tau'))\psi'_\alpha(\tau')} \\ &= \det(\boldsymbol{G}_0^{-1} - \boldsymbol{J}) \end{aligned} \tag{2.10}$$

where $\boldsymbol{G}_0$ denotes non-interacting green's function of the system.

$$\begin{aligned} \mathcal{G} &= -\frac{\partial \ln \det(\boldsymbol{G}_0^{-1} - \boldsymbol{J})}{\partial \boldsymbol{J}} = \frac{\partial Tr \ln(\boldsymbol{G}_0^{-1} - \boldsymbol{J})}{\partial \boldsymbol{J}} = (\boldsymbol{G}_0^{-1} - \boldsymbol{J})^{-1} \\ \therefore \quad & \boldsymbol{J} = \boldsymbol{G}_0^{-1} - \mathcal{G}^{-1} \end{aligned} \tag{2.11}$$

We can redefine the grand potential as a new functional of the green's function by the Legendre Transform of $-\ln \mathcal{Z}[J]$:

$$\Omega[\mathcal{G}] = -\ln \mathcal{Z}[\boldsymbol{J}] - Tr\boldsymbol{J}\mathcal{G} \tag{2.12}$$

$$\text{so that} \qquad \boldsymbol{J} = \frac{\partial \Omega[\mathcal{G}]}{\partial \mathcal{G}} \tag{2.13}$$

in the non-interacting case, because of Eq.2.11, the non-interacting grand potential Ω_0 can be obtained

$$\begin{aligned} \Omega_0[\mathcal{G}] &= -Tr\ln \mathcal{G}^{-1} - Tr[(\boldsymbol{G}_0^{-1} - \mathcal{G}^{-1})\mathcal{G}] \\ &= Tr\ln \mathcal{G} - Tr(\boldsymbol{G}_0^{-1}\mathcal{G} - 1) \end{aligned} \tag{2.14}$$

As we introduce interactions, the new grand potential Ω of the interacting system is different from Eq.2.14. The difference between Ω and Ω_0 is defined as $\Phi[\mathcal{G}]$, which is referred as the Luttinger-Ward (LW) functional. Therefore, the grand potential Ω of an interacting system can be written as

$$\Omega[\mathcal{G}] = -Tr\ln \mathcal{G}^{-1} - Tr(\boldsymbol{G}_0^{-1}\mathcal{G} - 1) + \Phi[\mathcal{G}]. \tag{2.15}$$

Taking the functional derivative on both sides of Eq.2.15 yields

$$\boldsymbol{J} = \mathcal{G}^{-1} - \boldsymbol{G}_0^{-1} + \frac{\partial \Phi[\mathcal{G}]}{\partial \mathcal{G}}. \tag{2.16}$$

If there is no source in the systems like the Hubbard model, the source term can be removed by setting $\boldsymbol{J} = \boldsymbol{0}$, so $\mathcal{G}$ becomes a green's function without the source $\boldsymbol{G}$. By doing this, one can immediately notice that the equation resulting

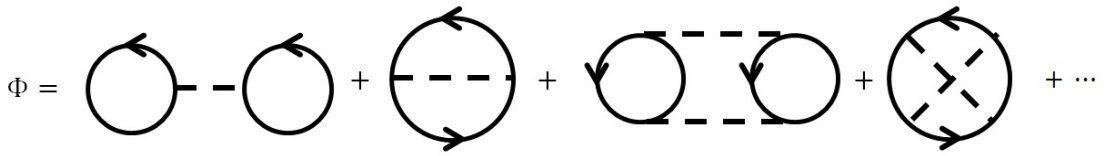

Fig. 2.1: The diagrammatic representation of the Luttinger-Ward functional, which is the sum of all the 2-particle irreducible diagrams.

from Eq.2.16 is the Dyson's equation $\boldsymbol{\Sigma} = \boldsymbol{G}_0^{-1} - \boldsymbol{G}^{-1}$, as long as $\boldsymbol{G}$ is a green's function representing the physical system described by H. Comparing the Dyson's equation to Eq.2.16 without the source, we have

$$\frac{\partial \Phi[\boldsymbol{G}]}{\partial \boldsymbol{G}} = \boldsymbol{\Sigma} \tag{2.17}$$

$$\Omega = -Tr\ln(\boldsymbol{G}_0^{-1} - \boldsymbol{\Sigma}) - Tr(\boldsymbol{\Sigma}\boldsymbol{G}) + \Phi[\boldsymbol{G}] \tag{2.18}$$

where $\boldsymbol{\Sigma}$ is the self energy of the interacting system, which satisfies the Dyson's equation $\boldsymbol{\Sigma} = \boldsymbol{G}_0^{-1} - \boldsymbol{G}^{-1}$. The Eq.2.18 is called the Baym-Kadanoff functional. According to Eq.2.17, the LW functional can be obtained by summing up all the 2-particle irreducible (2PI) diagrams wrt the green's function $\boldsymbol{G}$ (see Fig. 2.1). In theory, the LW functional in Eq.2.17, Dyson's equation and Feynman diagram for LW functional set up a self-consistent scheme for extracting exact green's function and thermodynamic properties of a correlated system:

1 Start from a trial green's function G

2 Construct the LW functional by summing up 2-particle irreducible diagrams

3 Find out self-energy Σ from Eq.2.17

4 Calculate a new green's function G

5 Iterate steps 2-5 until change in green's function is small enough

The green's function is the exact green' function of the system and can be used to extract other properties of the ground state.

An important property of the LW functional is that the functional dependence of $\Phi[\boldsymbol{G}]$ is universal when the interacting part is the same. At the non-interacting limit, the functional is zero, and for interacting cases, its functional form is determined by the summation of all the 2PI diagrams which include only U and $\boldsymbol{G}$. Therefore, the functional dependence of $\Phi[\boldsymbol{G}]$ is independent of the one-particle part of the Hamiltonian and completely determined by the interaction part. This suggests that as the interacting part of the Hamiltonian remains unchanged, the functional dependence of the LW functional is universal.

Potthoff functional

The LW functional shows a promising approach to a non-perturbative solution of correlated systems, but in practice, it is impossible to sum up all the 2PI diagrams to get a closed form for the LW functional and it is difficult to quantitatively calcualte the difference between two green's functions. Even for the

simplest Hamiltonian like the one-orbital Hubbard model, the general functional form of the LW functional is explicitly unknown.

Self-energy functional approach provides an alternative variational approach to solve a correlated system. The SFA is based on a functional $\boldsymbol{G}[\boldsymbol{\Sigma}]$ as a functional of self-energy $\boldsymbol{\Sigma}$ defined as the inverse of $\boldsymbol{\Sigma} = \boldsymbol{\Sigma}[\boldsymbol{G}]$. This requires that the self-energy functional $\boldsymbol{\Sigma}[\boldsymbol{G}]$ is locally invertible given that the system is not at the critical point of a phase transition [44]. We first define a functional F as the Legendre transform of the LW functional

$$\begin{aligned} F[\boldsymbol{\Sigma}] &= \Phi[\boldsymbol{G}] - Tr(\boldsymbol{\Sigma}\boldsymbol{G}) \\ \frac{\partial F[\boldsymbol{\Sigma}]}{\partial \boldsymbol{\Sigma}} &= \boldsymbol{G} \end{aligned} \tag{2.19}$$

so the grand potential becomes

$$\Omega[\boldsymbol{\Sigma}] = F[\boldsymbol{\Sigma}] - Tr\ln(\boldsymbol{G}_0^{-1} - \boldsymbol{\Sigma}) \tag{2.20}$$

one can immediately find that

$$\frac{\partial \Omega[\boldsymbol{\Sigma}]}{\partial \boldsymbol{\Sigma}} = 0 \Leftrightarrow \boldsymbol{G}[\boldsymbol{\Sigma}] = (\boldsymbol{G}_0 - \boldsymbol{\Sigma})^{-1} \tag{2.21}$$

Therefore, the functional $\Omega[\Sigma]$ is stationary at the physical self-energy and its value equals the exact grand potential of the system. This is the basic idea of the self-energy functional approach.

Because of universality of the functional form of the LW functional, its Legendre transform $F[\boldsymbol{\Sigma}]$ is consequently universal as long as the interacting term

is unchanged. In other words, if we introduce a reference system with Hamiltonian $H' = H_0(\boldsymbol{t}') + H_I(U)$, in which $H_I(U)$ is the same as that in the original system, so that the Hamiltonian has exactly the same interacting terms but different non-interacting (one-particle) terms. Eq.2.20 can be rewritten in the reference system as

$$\Omega[\boldsymbol{\Sigma}_{\boldsymbol{t}'}] = F[\boldsymbol{\Sigma}] - Tr\ln(\boldsymbol{G}_0'^{-1} - \boldsymbol{\Sigma}_{\boldsymbol{t}'}) \tag{2.22}$$

where the subscript $\boldsymbol{t}'$ denotes the hopping matrix in the reference system with one particle term $\boldsymbol{t}'$. $\Omega_{\boldsymbol{t}'}$ is stationary at physical self-energy $\Sigma = \Sigma_{\boldsymbol{t}'}$ and in Eq.2.20, Ω is stationary at $\Sigma = \Sigma(\boldsymbol{t})$. Combining Eq.2.20 and Eq.2.22, since the both functionals $\Omega_{\boldsymbol{t}'}$ and Ω share the same part $F[\boldsymbol{\Sigma}]$, one obtains the Potthoff functional

$$\begin{aligned}\Omega[\boldsymbol{\Sigma}] &= \Omega[\boldsymbol{\Sigma}_{\boldsymbol{t}'}] + Tr\ln(\boldsymbol{G}_0'^{-1} - \boldsymbol{\Sigma}_{\boldsymbol{t}'}) - Tr\ln(\boldsymbol{G}_0^{-1} - \boldsymbol{\Sigma}) \\ &= \Omega[\boldsymbol{\Sigma}_{\boldsymbol{t}'}] + Tr\ln(\boldsymbol{G}_0'^{-1} - \boldsymbol{\Sigma}_{\boldsymbol{t}'}) - Tr\ln(\boldsymbol{G}^{-1})\end{aligned} \tag{2.23}$$

This functional is exact as long as the hopping matrix $\boldsymbol{t}'$ and $\boldsymbol{t}$ are both defined in the same lattice space and the functional can be evaluated by searching for the stationary points to provide the physical grand potential. The Potthoff functional $\Omega[\boldsymbol{\Sigma}]$ indicates if there is a reference system that can be solved exactly, *i.e.*, the self-energy, green's function and grand potential can be obtained exactly at any $\boldsymbol{t}'$. The physical ground state can be extracted from the Potthoff functional exactly. However, in practice, systems that can be solved exactly are all smaller than

the original system, so $\boldsymbol{t}'$ only belongs to a subspace of $\boldsymbol{t}$. That means the result obtained from evaluating Eq.2.23 is not exact but an approximation to the ground state of the original system.

2.2.2 Variational Cluster Approximation (VCA)

An important part of the SFA requires a reference system that can be solved exactly to evaluate the stationary point of the self-energy functional $\Omega[\boldsymbol{\Sigma}]$, so the selection of the reference system is very critical. VCA method creates a natural way to introduce the reference system: a superlattice of identical clusters which are decompositions of the original lattice with the same interactions. Each cluster can be solved exactly, and the inter-cluster hoppings are introduced by the quantum cluster method [45] which also involves relations between parameters in the original system and in the superlattice (see Fig.2.2). This method, based on SFA theory with a reference system consisting of identical clusters, is called the variational cluster approximation, which can calculate the approximate ground state properties such as the green's function and grand potential.

Broken symmetries

One major drawback of the VCA is that it cannot treat spontaneously broken symmetry explicitly, because the self-energy space of the VCA reference system is

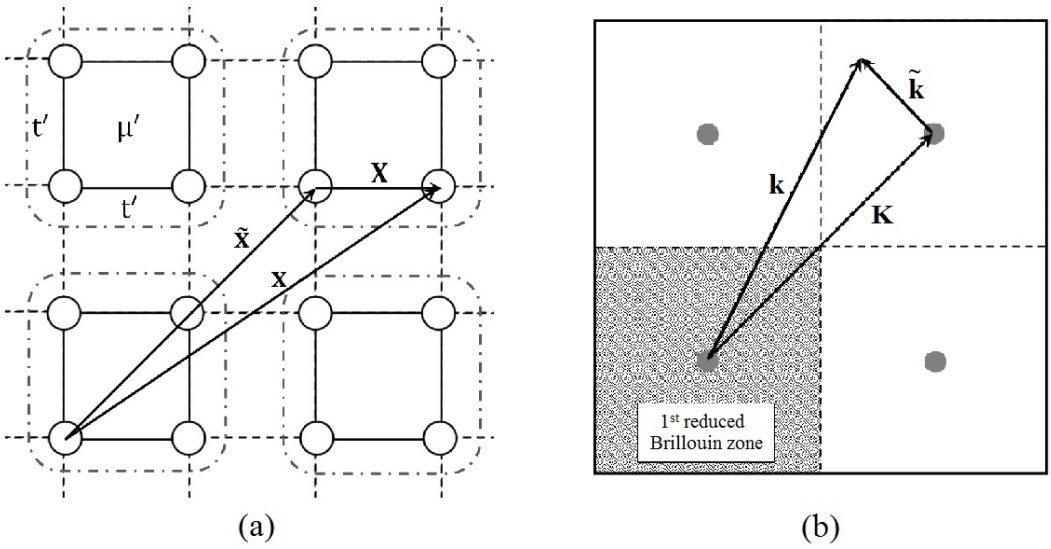

Fig. 2.2: A illustration of a reference system: (a) The whole lattice in the real space is divided into identical clusters with L sites (2×2 clusters with $L = 4$ in this figure) with the hopping parameter t' between the nearest atoms which is considered a variational parameter. The upper-case letters represent lattice vectors within a cluster and the tilded letters denote a vector connecting the origins of two lattices. For example, $\boldsymbol{x} = \boldsymbol{X} + \tilde{\boldsymbol{x}}$. (b) The whole square represents the first Brillouin zone (FBZ) in the reciprocal space and the shaded square denotes the reduced first Brillouin zone (RFBZ) of the superlattice of clusters. The upper-case letters are used for vectors between origins of two RFBZs and the tilded letters represent the momentum vectors within a RFBZ. For example, $\boldsymbol{k} = \boldsymbol{K} + \tilde{\boldsymbol{k}}$. The above definitions are used throughout the dissertation.

restricted in the cluster size, which cannot include long range ordering. In order to represent long range spontaneously broken symmetry, one can introduce a fictitious symmetry-breaking field in the reference system. An extra term representing the effect of the corresponding symmetry breaking is added to the reference Hamitonian. The fictitious field in the extra term is then subjected to be optimized in the Potthoff functional just like in mean field theory. The following show two examples of fictitious fields:

1) Néel Antiferromagnetism (AF)

$$H'_{AF}(M) = M \sum_{\boldsymbol{R}} e^{-\boldsymbol{Q}\cdot\boldsymbol{R}}(n_{\boldsymbol{R}\uparrow} - n_{\boldsymbol{R}\downarrow}) \tag{2.24}$$

where M denote the strength of AF fictitious field and $\boldsymbol{Q}$ is the AF ordering wave vector which indicates the symmetry of the magnetic ordering and is different in different types of AF phases. For the Néel type AF, $\boldsymbol{Q} = (\frac{\pi}{2}, \frac{\pi}{2})$.

2) Superconductivity

$$H'_{SC}(\Delta) = \sum_{\boldsymbol{r}\boldsymbol{r'}} \Delta_{\boldsymbol{r}\boldsymbol{r'}}(c_{\boldsymbol{r}\uparrow}c_{\boldsymbol{r'}\downarrow} + H.c.) \tag{2.25}$$

where Δ is the pairing function which is different from different types of superconductivity. For example, $d_{x^2-y^2}$ pairing corresponds to $\Delta_{\boldsymbol{r}\boldsymbol{r'}} = \Delta\cos(2\theta)$ where θ is the angle of the vector $\boldsymbol{r'} - \boldsymbol{r}$ *w.r.t.* the positive x direction. s pairing wave has $\Delta_{\boldsymbol{r}\boldsymbol{r'}} = \Delta\delta_{\boldsymbol{r}\boldsymbol{r'}}$

Fig.2.3 shows results of superconductivity studied by involving the SC fictitious field Δ as shown in Eq.2.25. This treatment of spontaneously broken

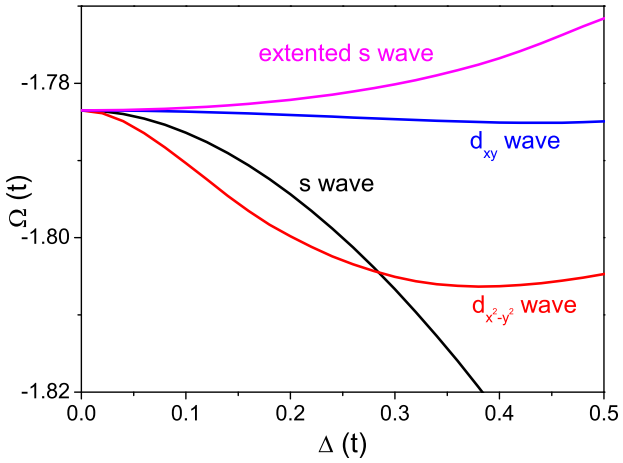

Fig. 2.3: The spontaneous superconducting states with s, extended s, $d_{x^2-y^2}$ and d_{xy} gap symmetries are tested in the Hubbard model on a square lattice with $U = 8$ and $\mu = 1.2$ at $T = 0$. The Potthoff functional Ω is plotted versus SC fictitious field Δ. The figure shows that only $d_{x^2-y^2}$-wave and d_{xy}-wave superconducting states can exist in the square lattice based Hubbard model. $d_{x^2-y^2}$-wave SC state is more stable compared to d_{xy}-wave SC state, since $d_{x^2-y^2}$-wave SC state has a lower grand potential.

symmetry has been testified in different systems. For example, the Néel AF state is systematically studied by VCA with an AF Weiss field in Ref. [46] and the SC fictitious field is used to study the SC state in Ref. [47].

Translational symmetry

Another issue is that the cluster decomposition breaks the translational symmetry of the original system. The consequence is that the green's function of the final result is not fully translationally invariant. Therefore, after we obtain the ground state from the VCA calculation, an additional step is needed to restore the translational symmetry. Such symmetrization is achieved by making transform of the green's function based on cluster superlattice:

$$G(\boldsymbol{k},\omega) = \frac{1}{L}\sum_{\boldsymbol{R},\boldsymbol{R'}} e^{-i\boldsymbol{k}\cdot(\boldsymbol{R}-\boldsymbol{R'})} G_{\boldsymbol{R}\boldsymbol{R'}}(\tilde{\boldsymbol{k}},\omega) \tag{2.26}$$

When the translationally symmetric green's function is obtained, the one particle excitation spectra $A(\omega,\boldsymbol{k})$ and the density of states $\rho(\omega)$ can be easily calculated

$$A(\boldsymbol{k},\omega) = -2\lim_{\eta\to 0^+} \Im G(\boldsymbol{k},\omega+i\eta) \tag{2.27}$$

$$\rho(\omega) = -\frac{2}{N}\sum_{\boldsymbol{k}} \lim_{\eta\to 0^+} \Im G(\boldsymbol{k},\omega+i\eta) \tag{2.28}$$

Thermodynamic consistency

There are normally two methods to get the electronic density n: 1) one can differentiate the grand potential Ω w.r.t the chemical potential μ: $n = -\frac{\partial\Omega}{\partial\mu}$; 2) n can be obtained by integrating the one particle green's function over the momentum and frequency space: $n = \int d\omega \sum_{\boldsymbol{k}} \boldsymbol{G}(\boldsymbol{k},\omega)$. Thermodynamic consistency means that the two methods yield the same result. The derivative in the first method contains two parts: the *explicit* μ dependency in the expression green's function

and *implicit* μ dependency in the self-energy. The explicit dependency can be shown to yield the same equation as the second method and the implicit dependency usually is not zero unless the system is at the true ground state, so the two method usually cannot achieve the same results. In order to restore thermodynamic consistency, a simple recipe is to add an extra term to the reference system $H_\epsilon = \epsilon \sum_{\boldsymbol{r}} c^+_{\boldsymbol{r}} c_{\boldsymbol{r}}$, where ϵ denotes the on-site energy of an electron in the reference system and it is set as a variational parameter. The discussions of thermodynamic consistency can be found in Ref. [48].

Steps of VCA calculations

In concluding this section, we provide the steps needed to conduct a VCA calculation and a schematic representation of a VCA calculation in Fig. 2.4:

1. Divide the original lattice into identical clusters.

2. Add a fictitious mean field if any long range order is required.

3. Calculate the Potthoff functional in Eq.2.23.

4. Implement an iterative variational process until a stationary point in the Potthoff functional is found.

5. Symmetrize the green's function and derive the properties of the system from it.

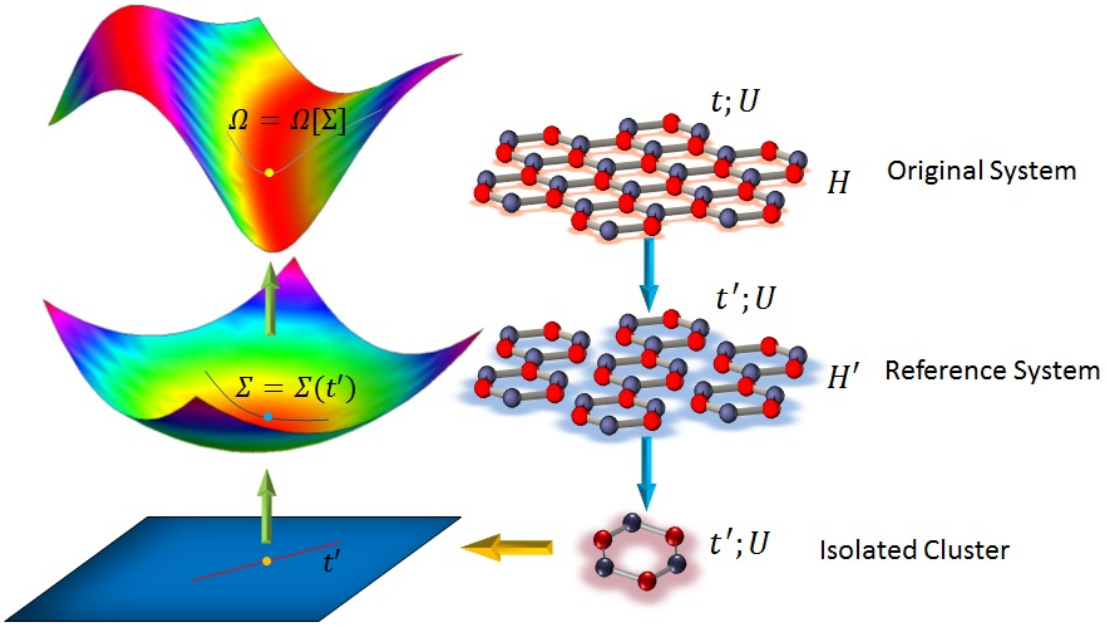

Fig. 2.4: A schematic representation of the calculation process of variational cluster approximation.

Chapter 3

Phase separation instability in isolated clusters

3.1 Introduction

Most theoretical or numerical methods in condensed matter physics are based on the assumption that particles (electrons or holes) distribute homogeneously throughout the material, so that these approaches can deal with problems within the momentum space. However, when one is dealing with inhomogeneous electronic systems, most momentum space approaches are no longer valid, so some real space techniques are essential. When Inhomogeneities happen, the length scales of inhomogeneous patterns are usually finite [49], even only at nanoscales; and it is well known that the coherence length of high temperature superconductor is only 3 to 4 lattice spacings. These facts suggest that studies of finite clusters may extract meaningful perspective of strongly correlated systems and especially the electronic inhomogeneity. The small-size clusters with optimized shapes may be one of the few *solid grounds* available for studies of large strongly correlated

lattices [50,24,51]. In this chapter, the cluster calculations are used to explore the basic ideas of electronic phase separation.

Clusters with the optimal shapes were proposed by Betts in his papers [52,53] that studied the exact ground state properties of the infinite two-dimensional (2d) Heisenberg model. These clusters are called Betts cluster/lattice and expected to reduce the frustrations coming from cluster size and different boundary conditions [53]. Each of them can be enclosed in a square shape although some of them do not have all the symmetry properties of the infinite square lattice. An infinite square lattice can be tiled by squares of L-site Betts clusters with edge vectors which represent displacements of one vertex to the equivalent vertex in the neighboring tile with which it shares an edge (See Figure 3.2). Studies of finite clusters with periodic boundaries and next nearest neighbor hopping can play an important part in testing the reliability of the results drawn from finite-size systems [54,55].

In this chapter, we address two specific issues: (i) check how exact calculations in finite Betts-cluster-based lattice are consistent with electronic inhomogeneities obtained from calculations of 2×2 and 2×4 clusters and, (ii) analyze the effect of lattice frustration on phase separation instabilities in bipartite geometry driven by the next nearest neighbor coupling.

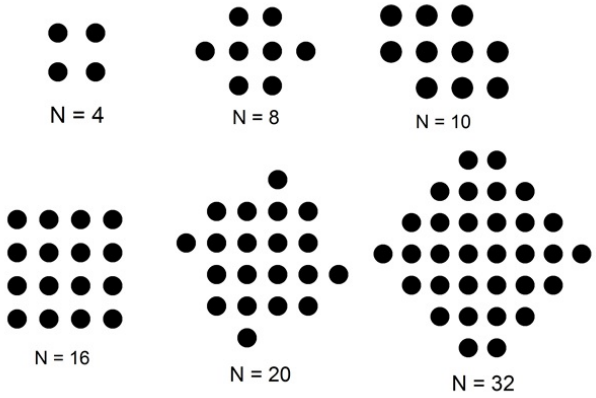

Fig. 3.1: Schematic representations of some different Betts clusters from Ref. [56]. Each of them can be enclosed in a square shape although some of them do not have the full symmetry properties of the infinite square lattice [52].

3.1.1 Model

We consider the extended Hubbard model in this capter

$$H = -\sum_{i,j;\sigma} t_{ij} c^{+}_{i\sigma} c_{j\sigma} + U \sum_{i} n_{i\uparrow} n_{i\downarrow} \tag{3.1}$$

where summation over i and j in Eq.3.1 goes through all lattice sites L with coupling integral t_{ij}

$$t_{ij} = \begin{cases} t & \text{if } i,j \text{ are nearest neighbors,} \\ t_{nnn} & \text{if } i,j \text{ are next-nearest neighbors,} \\ 0 & \text{otherwise.} \end{cases} \tag{3.2}$$

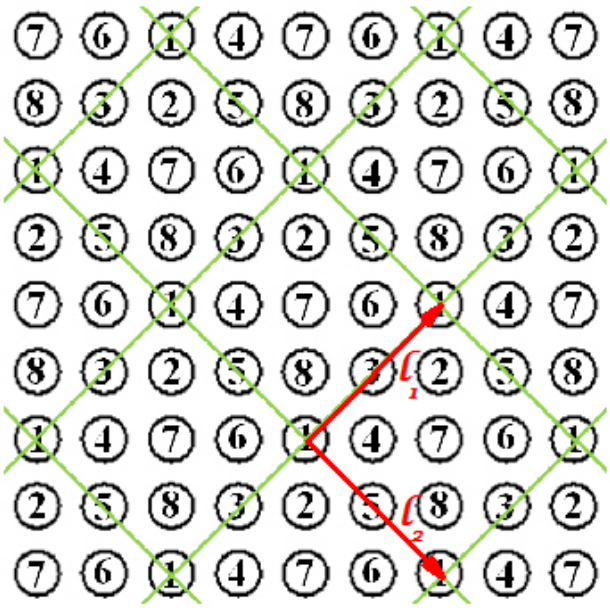

Fig. 3.2: The 8-site finite unit cell (*plaquette*) for the square lattice. When repeated periodically, it can fill the entire (*infinite*) space. The cells have $\mathbf{l}_1$ and $\mathbf{l}_2$ edge vectors, (2,2) and (2,-2), as defined in Ref. [52].

and $U > 0$ is the on-site Coulomb interaction. The energies are measured with respect to $t_{nn} > 0$, which is set to 1 everywhere, unless otherwise stated.

3.2 Results

3.2.1 Phase separation instabilities

We consider L=8 and 10 site Betts clusters where the dimensions of the Hilbert spaces are 4^8 and 4^{10} respectively. An exact diagonalization along with the Lanczos algorithm [43] is employed to evaluate the relevant, low lying eigenstates at all filling (doping) values. These eigenstates are used in Sec. 3.2.1to extract the charge pairing gaps and corresponding pairing instabilities of the model.

Charge pairing instability

We identify charge pairing behavior at zero temperatures in a L-site cluster by defining a charge gap $\Delta^c(N,T)$ at a given U in a particular doping region:

$$\Delta^c(N,T) = E(N+1,T) + E(N-1,T) - 2E(N,T) \tag{3.3}$$

where $E(N,T)$ is the lowest canonical many body energy for an N-electron state at a fixed temperature T. This charge gap determines the stability of an $N-$electron state compared to an equal admixture of $(N+1)-$ and $(N-1)-$electron states. As shown in Figure 3.3, the electron number in clusters can fluctuate while keeping an average number $\langle N \rangle$ unchanged. This schematic picture for $\langle N \rangle = 7$ illustrates

formation of variation of electron concentrations among clusters. The number of electrons in two $N = 7$ clusters which represent the uniform state can fluctuate so that they become an equal distribution of $N = 6$ clusters and $N = 8$ clusters which is a mixed state (electronic phase separation). If the latter configuration has a low energy ($\Delta^c < 0$), it will create inhomogeneous electron variations.

When phase separation happens, it seems electrons or holes are forced to concentrate in a single cluster, which effectively introduces an attractive force between the electrons or holes. The effective attraction may produce some pairing effects between electrons or holes, and this is one of the reasons that some theorists proposed that there might be a connection between electronic phase separation and cooper pairs that create the superconductivity [22,57,24]. The absolute value of the *negative* charge gap represents how hard it is to break the pairing, because it is the energy needed to convert the phase separated clusters into uniform states. Therefore the absolute value of the negative charge gap is also defined as the pairing gap or pairing energy in cluster calculation [24,25,58]. Note that when the charge gap is positive, the pairing gap is defined as zero. This definition will be used throughout the thesis.

Depending on the strength of the on-site electron-electron repulsion U, this charge gap can be positive $\Delta^c > 0$ or negative $\Delta^c < 0$. Physically, $\Delta^c > 0$ manifests a stable uniform phase, while $\Delta^c < 0$ describes a electronic phase separation instability with inhomogeneous electron distributions. Thus, for a given chemical

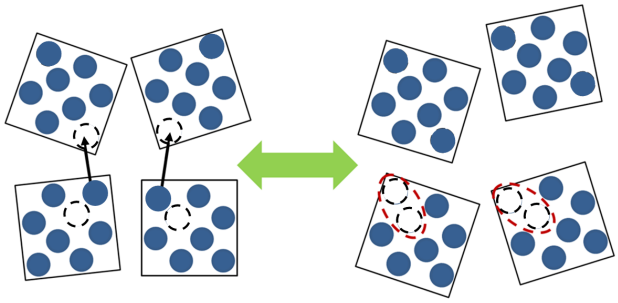

Fig. 3.3: Schematic drawing of hole (electron) redistribution within Hubbard nanoclusters with one hole of half-filling in the grand canonical ensemble of 8-site clusters at low temperatures. The state on the left is an ordinary state at $N = 7$ per unit cell. Notice that the spontaneous fluctuations in particle number, near the average $\langle N \rangle = 7$, are energetically favorable and make electron redistribution across the ensemble of clusters possible even without direct contact (hopping) between them. When $\Delta^c > 0$, the hole localization on separate clusters corresponds to a homogeneous stable $N = 7$ state. When $\Delta^c < 0$, the mixture of $N = 6$ and half-filled $N = 8$ inhomogeneous cluster configurations on the right are energetically preferred.

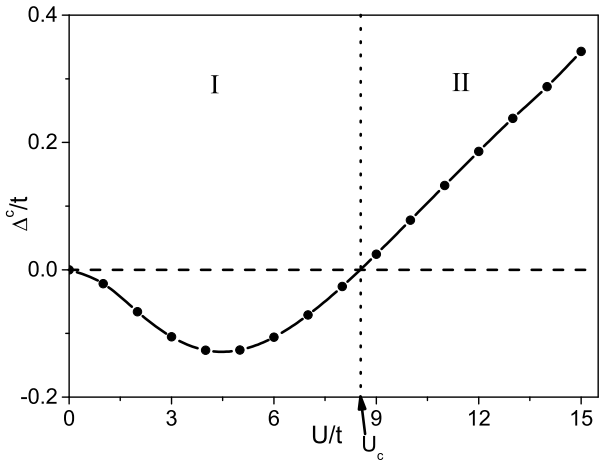

Fig. 3.4: The *canonical* charge Δ^c in the ensemble of the 8-site Betts cluster for $N = 7$ as a function of U at $t_{nnn} = 0$ and $T = 0$. Phase I is a phase with a negative charge gap at $U < U_c$ which describes the phase with inhomogeneous electron distribution. Phase II is a homogeneous phase with uniform electron concentration.

potential and temperature in the grand canonical ensemble, electrons are allowed to be redistributed among the clusters to optimize their free energy. Thus, on the left of Figure 3.3, a homogeneous Mott-Hubbard state with electron-hole pairing is preferred in the positive charge gap ($\Delta^c > 0$) region, while in the negative gap region ($\Delta^c < 0$) on the right, an inhomogeneous phase with hole-rich ($N = 6$) and hole-poor ($N = 8$ half-filled) clusters becomes energetically favorable. The charge gap Δ^c at $T = 0$ is plotted as a function of U in Figure 3.4 for $N = 7$. The charge gap in Figure 3.4 vanishes ($\Delta^c(U_c) = 0$) at $U = 0$ and also at a particular U value, *i.e.,* $U_c = 8.52$, which represent the transition between the uniform phase to separated phase. Compared to results of the 2×2 square cluster [24], the negative charge gap ($\Delta^c < 0$) for the 8-site clusters with electron number $N = 7$ has a larger maximum pairing energy and a larger transition U_c value. The homogeneous state with $\Delta^c > 0$ is stable at all $U > U_c$ (shown in Fig. 3.4) while for $0 < U < U_c$, the ground state consists of redistribution of electrons indicating a tendency toward phase separation [59].

Square symmetry

Broken symmetry of the two-dimensional planar geometry in various finite-size Hubbard clusters plays a crucial role in determining the pairing symmetry and superconducting properties. Our results in various square (bipartite) geometries

show that pairing properties strongly depend on the cluster symmetry. The gap behavior in the 8-site Betts cells is different from the 2×4 ladder [25,60]. For comparison, in Figure 3.5, we show the exact charge gap with reduced square symmetry in the 10-site Betts lattice as a function of U. The region with a negative charge gap does not start from $U = 0$ any more and the maximum pairing energy is significantly larger. This figure also shows an oscillating gap due to the reduced square symmetry which resembles that of the 2×4 clusters [25]. Both the 2×4 ladder and the 10-site Betts lattice (with edge vectors (1,3) and (3,-1)) have lower symmetries than the 8-site Betts cell (with edge vectors (2,2) and (2,-2)) and we believe that the oscillations in the charge gap (as a function of U) are related to this. Although a positive charge gap appears at very small U values, the evolution of the gap is quite similar to our results obtained in other clusters. Thus, Betts 8- and 10-site clusters provide strong support for electron instabilities and nanoscale inhomogeneities found in the generic 2×2 and 2×4 clusters in [25,60] and reproduced later [61].

Finite temperature effects

Finite temperature is introduced by using the grand canonical ensemble for clusters. The contour lines for the charge gap as a function of T and U, along which the gap attains a constant value c ($\Delta^c(U,T) = c$) defines the contour map

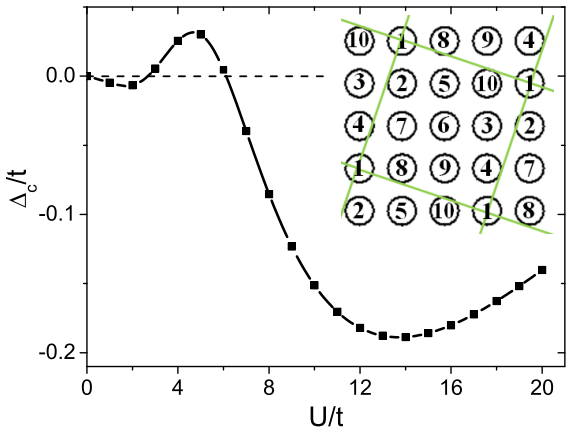

Fig. 3.5: A plot of the charge gap Δ^c in the 10-site Betts cell at $N = 9$ as a function of U at $t_{nnn} = 0$ and $T = 0$. In contrast to the 8-site lattice, optimized pairing is shifted to larger U values and a positive charge gap appears at very small U values. This is due to the reduced symmetry of 10-site geometry (see the inset) compared with the 8-site lattice (see Sec. 3.2.1).

in Figure 3.6. The slice cut of the vanishing gap ($c = 0$) at finite temperatures ($\Delta^c(U,T) = 0$) defines the boundary between positive and negative charge gap, *i.e.*, the phase boundary between the uniform phase and separated phase, which is marked by the solid line in Figure 3.6. The magnitude and range of negative charge gap at a given temperature shrink as temperature increases and finally disappear at a certain temperature (about $T = 0.16$), indicating that the pairing and phase separation is a low temperature phenomenon.

3.2.2 Next nearest neighbor coupling

In many real materials (such as the cuprates), the contribution of hopping among next nearest neighbors (nnn) can be important because the presence of nnn breaks particle-hole symmetry [62]. Therefore, a study in the Hubbard model with $t_{nnn} \neq 0$ (See Eq. 3.2) might give a more realistic physical picture related to real materials. In this section, we discuss the effects due to a nonzero t_{nnn}. Because t_{nnn} in real material is usually much smaller than t parameter we only show results for $-0.3 < t_{nnn} < 0.3$. Below we will find conditions under which broken C_4 symmetry in frustrated Betts cells with $t_{nnn} \neq 0$ can be harmful or favorable for pair binding.

At zero temperature, charge gaps at one hole off half-filling (contour plots or isolines) for different t_{nnn} and U values are shown in Figure 3.7. The charge gap behavior in the region $-0.3 < t_{nnn} < 0.3$ is similar to that found in section 3.2.1: A negative charge gap, representing charge pairing, can be found at relatively small

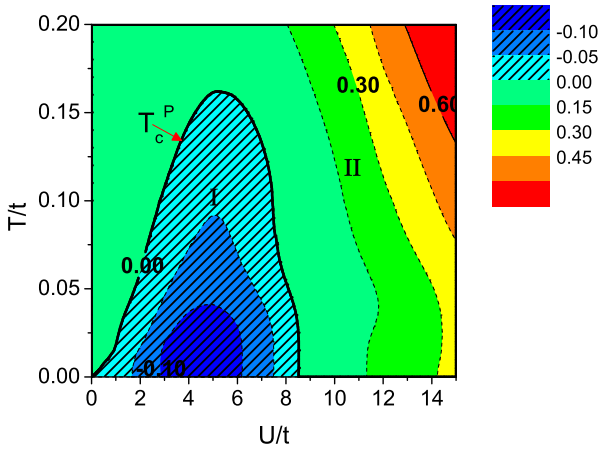

Fig. 3.6: A contour plot of charge gap in the 8-site (periodic) Betts cluster at $N = 7$ as a function of Coulomb repulsion U and temperature T. As T increases, the region of negative charge gaps becomes smaller and the crossover point $U_c(T)$ shifts to lower U values. The negative gap disappears completely at about $T = 0.16$. The solid boundary in the figure denotes the contour $T_c^P(U)$ at which the charge gap vanishes ($\Delta^c = 0$). Phase I with a shaded pattern is the electron-electron pairing phase. Phase II without a shaded pattern is the homogeneous phase.

U values. The bold line in Figure 3.7 shows where the charge gap becomes zero, which defines a phase boundary between inhomogeneous phase and homogeneous phase. As t_{nnn} increases from negative (opposite sign as that of t) to positive (same sign as that of t), the boundary shifts to larger U values and the magnitude of the pairing gap becomes larger. This is because that the hopping between next nearest neighbors are energetically unfavorable for the half-filled antiferromagnetic state since the next nearest neighbors have the same spin direction. When holes are created in the antiferromagnetic background, hopping between next nearest neighbors will become more active and will have a measurable effect on the ground state. Depending on the sign of t_{nnn}, it will make the energy of the inhomogeneous state become higher ($t_{nnn} < 0$) or lower ($t_{nnn} > 0$). Therefore a positive t_{nnn} makes separated phase ground state more energetically favorable and enhances the negative charge gap. In spite of this introduced frustration in the square system, pairing can be enhanced by introducing appropriate next-nearest-neighbor couplings ($t_{nnn} > 0$).

At fixed U, the plot of charge gaps vs. different t_{nnn} is shown in Figure 3.8. In the $t_{nnn} < 0$ region, charge gaps are linearly dependent on t_{nnn}, while they show nonlinear behavior when $t_{nnn} > 0$. The charge gap for $T = 0$ is consistent with the conclusions drawn from ground state calculations in $t - t' - J$ model at $t' < 0$ and $t' > 0$ [63]. This linear behavior of charge gap at negative t_{nnn} suggests that the variation of the charge gap for small nonzero $|t_{nnn}|$ can be obtained from

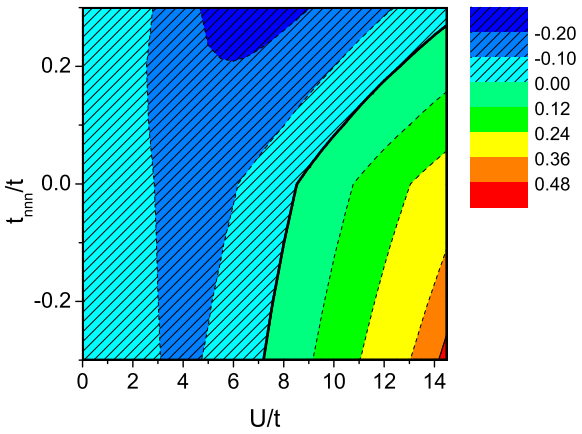

Fig. 3.7: A contour plot of charge gap Δ^c for different U and t_{nnn} at $T = 0$. As t_{nnn} increases the crossover point shifts to a larger U values and the maximal charge gap width increases as $t_{nnn} > 0$ but remains the same as $t_{nnn} < 0$. The negative gap region is shaded.

linear extrapolation from the case with zero t_{nnn}, which makes further research on next nearest hopping easier. Further calculations show that the linear behavior is lost when t_{nnn} is positive and large; since t_{nnn} has already exceeded the range where t_{nnn} is reasonably small (as the hopping between next nearest neighbors), we will not discuss it in this article. Figure 3.8 also shows that the linear slope approaches zero as the magnitude of the gap approaches its maximum (antinode) value (around $U = 4$), which indicates that, although negative t_{nnn} drives the phase separation transition point to a smaller U value, it does not affect the maximum gap value significantly.

3.3 Summary

We have discussed the charge gap in the 8- and 10-site Betts clusters subject to periodic boundary conditions. This work provides ample evidence that such phase separation instabilities do exist and are robust at the 8- and 10-site cluster sizes in the ground state and at finite temperatures. An important question is whether the obtained electronic phase separation will continue to exist in the two-dimensional lattice as the cluster size increases, especially, in the thermodynamic limit. As exact calculations cannot go up to clusters large enough to eliminate size effects, the periodic Betts cells are considered to be the best optimal structures that can minimize and reduce edge effects. The key intrinsic properties of an infinite square lattice can be extracted from exact calculations in finite Betts

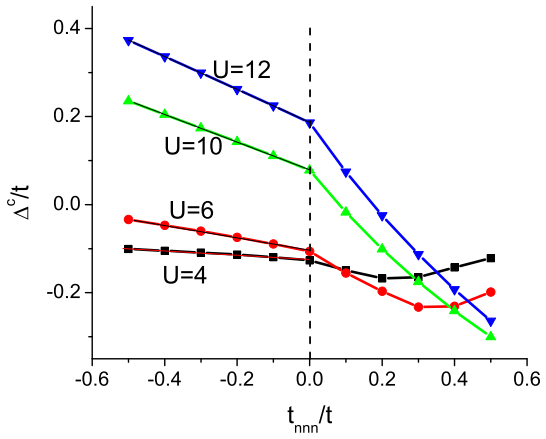

Fig. 3.8: Charge gap at fixed U value for different t_{nnn}. A linear relation is found in the negative t_{nnn} region. When $t_{nnn} > 0$, the variation of the gap is not linear. This picture suggests that clusters with different signs for the next nearest neighbor hopping have different effects on the spectral properties and electron charge pairing.

lattices [54]. For example, the extrapolated ground state energy from 8- and 10-site Betts cells per site at half-filling at large U is quite close to the existing analytical result in thermodynamical limit, $-1.15 \times \frac{4t^2}{U}$ [64]. The basic scenario of electronic phase separation reproduced in small Betts lattice near half-filling, can be valid also in larger size Betts lattices. The introduction of next nearest neighbor hopping shifts the quantum crossover points but cannot completely eliminate the conditions necessary for electronic inhomogeneities.

Chapter 4

Simulation of pairing gap modulations

4.1 Introduction

A challenging application of charge gap calculations to the inhomogeneous strongly correlated system is to use the concept of the pairing gap introduced in Chapter 3 to explain the gap modulation found in $Bi_2Sr_2CaCu_2O_{8+\delta}$ ($Bi-2212$). It is believed that the superconductivity in cuprate materials originates from the electron correlations in the CuO_2 planes. Although all the cuprate families share the same CuO_2 plane, the maximum T_c varies dramatically from one cuprate family to another [65]; for example, $La_{2-x}Ba_xCuO_4$ has a $T_c = 30K$ [66] while $HgBa_2Ca_2Cu_3O_{8+\delta}$ at high pressure has a T_c up to over $150K$ [67]. Such a large variation is unlikely to be caused by the electronic interactions in the CuO_2 plane, but it is most probably due to different atomic structures between the planes and their indirect effect on the electronic structure in the CuO_2 plane.

Recently, More systematic experimental studies have been done on $Bi2212$

[68–70] using Scanning Tunneling Microscopy (STM). This material has a complicated superstructure modulation (supermodulation) which is known to have a strong effect on the position of atoms between CuO_2 planes but almost no effect on the CuO_2 plane [70]. Slezak et al. measured the local energy gap by STM with atomic resolution and found that the energy gap also has a modulation with the same periodicity as the structural supermodulation [68]. It is important to know that the nature of energy gap measured by STM is still ambiguous. Right now, most people tend to believe that the gap is actually the so-called pseudogap that has been widely discussed in cuprate materials [10]. In this chapter, we do not intend to clarify the ambiguity, but focus only on the pairing gap which is clearly defined in Chapter 3.

Inspired by the observation of gap modulation, several theoretical proposals have been put forward by introducing variations of coupling constants on a phenomenological level, or applying the conventional BCS theory [71–75]. In this chapter, we report the results of a microscopic study of the pairing gap modulation for repulsive electrons within individual unit cells in real space for various changes of the structure and the chemical potential. We argue that the pairing correlations are modulated by variations of the charge density and the out-of-plane effect.

4.2 Model

The Hubbard model based on clusters is used for this study, because the lattice modulation needs the real-space calculation. The cuprate materials have very complicated out-of-plane structures which cannot be represented in one-band Hubbard model, because only (dressed) coppers are considered as vertices in one-band Hubbard model while no oxygen atoms explicitly show up in the model [76]. the simplest way to simulate the out-of-plane layers is to use a out-of-plane vertex which allow electrons/holes hopings and carry an on-site Coulomb interaction. Note that this single vertex does not represent any real atoms but it is a representation of all the out-of-plane effects, so do not consider it as an oxygen atom. Such a model looks like a pyramid, and different positions of the apical vertex denote different configurations of out-of-plane atoms.

Therefore, We begin with the canonical single band Hubbard model on a pyramid cluster (as shown in Fig. 4.1).

$$H = -t \sum_{\langle i,j\rangle\sigma} (c^{+}_{i\sigma} c_{j\sigma} + H.c.) - \sum_{i\sigma} t'_i (a^{+}_{\sigma} c_{i\sigma} + H.c.) + \sum_{i} U_i n_{i\uparrow} n_{i\downarrow} \qquad (4.1)$$

Here, $c_{i\sigma}$ ($c^{+}_{i\sigma}$) is the electron destruction (creation) operator at the basal sites with spin σ (or magnetic sublevel), while a_σ (a^{+}_{σ}) is the same operator at the apical site. The first term indicates the hopping between the nearest basal sites i and j ($\langle i, j\rangle$ denotes the nearest neighbor sites) with the same hopping parameter t. The second term describes hopping between the apical site and the basal site i with a hopping amplitude t'_i. In addition, $U > 0$ is the on-site Coulomb interaction. In practice, the hopping within the plane should be much bigger than that of the

out-of-plane atom, *i.e.* $t_i' \ll t$. In this chapter, the energies are measured with respect to $t > 0$ unless otherwise stated. The cluster can be solved exactly for all the eigenvalues and eigenvectors [24]. The apical site can exchange holes with all the basal sites, so displacements of the top site within the cluster will affect the planar electronic structures.

The pyramid structure breaks the electron-hole symmetry, so the sign of the hopping amplitude between the nearest neighbor sites leads to distinct changes of the electronic structure [26]. The results of these calculations strongly depend on the signs of t and t_i'. Here the pyramidal non-bipartite geometry is defined by choosing $t > 0$ as the hopping connecting square (plaquettes) sites in the basal plane, and we consider various hopping parameters $0 < t_i' \ll t$ as hoppings between the apical site and the planar site i in the square base (Fig. 4.1).

4.2.1 Charge gaps and pairing gap

Numerical (exact) calculations of the energy levels E_N for the relevant electron number N are used to define charge gaps. The charge gap Δ^c at finite temperature is defined the same as the previous chapter:$\Delta^c(N,T) = E(N+1,T) + E(N-1,T) - 2E(N,T)$. The charge gap determines the stability of an $N-$electron state compared to an equal admixture of $(N+1)-$ and $(N-1)-$electron states (the average number of electrons for this mixture is still N). As discussed in Chapter 3, within certain range of U value, the charge gap can be negative ($\Delta^c < 0$) which

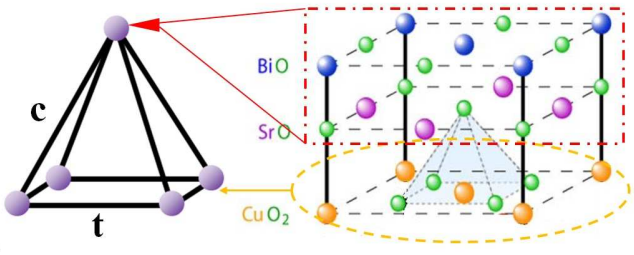

Fig. 4.1: A schematic picture of the pyramid cluster discussed in this work with an approximate visual aid indicating the attempted connection to the real crystal structure: in particular, at this approximate level, the apical site in the pyramid is expected to represent all the out-of-plane effects in the real crystal. The hopping parameters on the basal plane are denoted by t and the hopping parameter c $(= t_i)$ between the top site and basal sites can be independently varied. Here, all the energy parameters are measured in units of t.

implies the inhomogeneous distribution of electron concentrations. At the same time, because some electrons/holes are forced to concentrate within the same region (cluster), this create an effective pairing effect and a finite energy equal to the absolute value of negative charge gap is required to break the state. Therefore, we define a pairing gap as

$$\Delta^P = \begin{cases} -\Delta^c & \text{if } \Delta^c < 0, \\ 0 & \text{otherwise.} \end{cases} \tag{4.2}$$

The charge gap $\Delta^c(N,T)$ determines whether electrons in pisolated clusters prefer to distributed uniformly ($\Delta^c > 0$) or give rise to local charge inhomogeneity ($\Delta^c < 0$). The pairing gap $\Delta^P(N,T)$ corresponds to an effective electron pairing strength, so it can be positive or zero.

4.3 Results

We first testify the model with the simplest case and then discuss the effects of apical vertex when it is moving around its equilibrium position. When we have all the information regarding the apical site and its relation to the pairing gap, we are able to simulate the pairing gap modulation and fit the experimental results.

4.3.1 Square pyramids

High temperature superconductors have complex layered structures. For

example, there are various layers, bilayers or trilayers that can affect the superconductivity attributed to the Cu-O planes acting as *reservoirs* of electrons or holes. We attempt to model such complex structures with a simple pyramid having a square base and and an out-of-plane (apical) site. According to the definition of pairing gap Δ^P, a negative charge gap Δ^c is essential for Δ^P to be nonzero. We first consider the simplest case to test the validity of the model: a symmetric pyramidal cluster with equal hopping terms $t_i' = c$ $(i = 1, 2, 3, 4)$ between the apcial site and the all the basal sites, which are supposed to represent the CuO_2 planes (Fig. 4.1). The charge gap Δ^c at $T = 0$ as a function of coupling parameter c is shown in Fig. 4.2 at various U values and low temperatures, $T \to 0$ (in units of t) close to optimal doping for one hole of half filling, $N = 4$ (electron concentration $n = 0.8$). The energy gap vanishes in a multiparameter space of U and c. In the Fig. 4.2 plots with $U \leq 4$ provides strong evidence for the existence of such a level crossing, associated with electronic phase separation instability. For example, the charge gap at $U = 3$ vanishes at $c_{crit} = t'/t \approx 0.35$, which indicates a transition from electron pairing into Mott-Hubbard behavior. The negative charge gap $(\Delta^c < 0)$ corresponds to the pairing gap $\Delta^P = -\Delta^c$ in a square pyramid (with $t = 1$ in the basal plane), while for $c > c_{crit}$, the uniform ground state with $\Delta^c > 0$ is stable.

As shown in Fig. 4.2, as the hopping c increases but remains small (for example, $c < 0.34$ for $U = 3$), the value of the charge gap changes very slowly, which

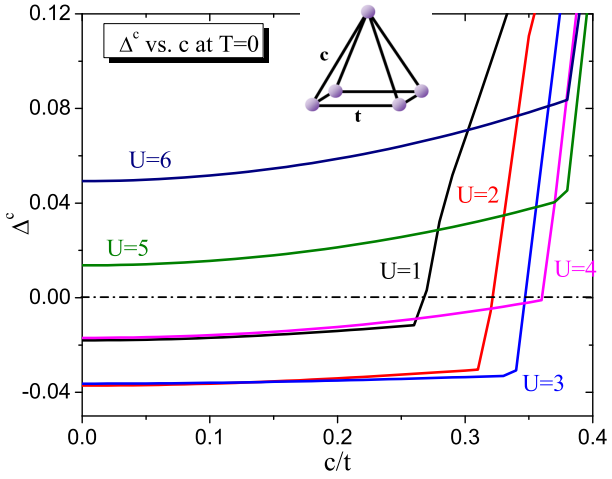

Fig. 4.2: A plot of charge energy gap versus intersite (apical) coupling c. When hoppings between the apical and the basal sites are all the same $t_i' = c$, the charge gap Δ^c is calculated as a function of c at several U values. The region $\Delta^c < 0$ has a ground state with a pairing gap $\Delta^P = -\Delta^c$. At relatively small c, the gap remains almost constant, which indicates that when the apical site is far from the base, the electronic state on the apical site cannot affect the pairing state on the base. When c is large enough, the dependence of $\Delta^c(c)$ becomes rather steep and beyond the transition value (c_{crit}) gap Δ^c becomes positive. This implies that coupling between the top and base (when apical site gets closer to the plane) can destroy electron pairing at the base. Note that at $U = 3$, the system has the largest magnitude of the negative gap covering the widest range of c.

corresponds to the case with the top site far from the basal plane. The result indicates that the presence of the apical site induces very small perturbations on the electronic state at the planar electronic state when it is far away. However, when c is large enough (for example, $c > 0.34$ for $U = 3$), there is a dramatic change and the charge gap becomes positive. This illustrates the case with the apical vertex close enough to the base, so the electronic state on the apical site greatly affects the electronic state on the basal plane and tends to destroy the electron pairing on the base as the apical site gets closer to the plane. Comparing to results of the 2×2 square geometries [26], we can conclude that the electronic structure of the basal sites contributes significantly to the formation of electron pairs, while the apical site tries to destroy such pairing by "sharing" holes/electrons with the basal sites. This result is consistent with the conclusion of Slezak et al. [68] who stated that the "pair density" is anti-correlated with the height of apical O atom. Given the consistency of this simple result, the pyramid may be a good candidate for studying local gap modulations. The pairing gap has the maximum magnitude and the widest range at $U = 3$, so we here consider the gap modulation for only $U = 3$.

The relation between apical site and next nearest neighbor site

Another feature of the pairing gap behavior in the pyramidal structure is that when the variations of c are small, the gap varies linearly with a very small slope.

It suggests that the apical effects at small c values can be treated by perturbations. This feature resembles the effect of small next nearest neighbor hopping in the square lattice. For the simplest case, assume all the apical hoppings are the same $c = t'$, and t_n is used to denote next nearest hopping. Both t' and t_n are small relative to t.

Assume that the ground state of a four-site cluster without next nearest neighbor is $|\psi\rangle$ and the ground state of an isolated apical atom is $|g\rangle$, so the first order correction due to the next nearest hopping is

$$\Delta E_n = \langle\psi|t_n \sum_{nnn} c_i^+ c_j|\psi\rangle \tag{4.3}$$

where $\sum_{nnn}$ means summation over all the next nearest neighbors. While, the first order perturbation due to the apical hopping is

$$\Delta E' = \langle g\psi|t' \sum_{nnn} c_i^+ (c \sum_m |m\rangle\langle m|c^+) c_j|g\psi\rangle \tag{4.4}$$

where $|m\rangle$ is the m^{th} state of the top atom. Comparing Eq. 4.4 and Eq. 4.3, $c\sum_m |m\rangle\langle m|c^+$ multiplication is the only difference. If $c\sum_m |m\rangle\langle m|c^+ = \mathbf{1}$, the two equation are equivalent. Usually, $|m\rangle$ can be state with no electron $|0\rangle$, one up spin $|\uparrow\rangle$, one down spin $|\downarrow\rangle$, or two spins $|\uparrow\downarrow\rangle$ and these four states build up a complete basis, so $\sum_m |m\rangle\langle m| = \mathbf{1}$. However, $c|m\rangle$ only include three terms $|0\rangle$, $|\uparrow\rangle$, and $|\downarrow\rangle$, so

$$\Delta E' = t' \sum_{nnn} (\langle g\psi|c_i^+ c_j|g\psi\rangle - \langle g\psi|\uparrow\downarrow\rangle\langle\uparrow\downarrow|g\psi\rangle) \tag{4.5}$$

Therefore, as long as the ground state of apical atom is not a two spin state, the effect on the ground state energy within the first order correction due to the apical atom is same as the next nearest hopping. It is hard to determine all the cases that the condition is satisfied, but some specific cases can be empirically found: (1) when hopping between the apex and the plane is small, the holes have very small probability to occupy the apical atom at the same time; (2) When the electron interaction is strong enough, the double occupancy is prohibited, but this case also causes the spin frustration because of the non-bipartite structure.

This equivalence between the two effects indicates that the influence of a far-away top site is like a bridge connecting the next nearest neighbor sites so that it perturbs the electronic state at the plane but does not significantly destroy the paired state. Slezak et al. observed a gap modulation of about 9% in their experiments which is large enough to address the destruction of electron pairs [68]. Such a big gap modulation is not suitable for a perturbation treatment.

4.3.2 Displacement of apical site

From the analysis of the previous section, we conclude that the best simulation conditions for the charge gap are $U = 3t$ and $t' > 0.34t$. The next step is to obtain the positional dependence of the hopping parameters. The hopping parameter between the top and the base is closely related to the distance between

the apical site and the basal site, *i.e.*, $t'_i = t'(r_i)$, where r_i is the distance between the apical site and the basal site i. In an ideal crystal, there is an equilibrium position r_i with the hopping parameter t'_0 that makes the system most stable. When the layers of atoms are present above the Cu-O planes, the position of the apical site can be perturbed with a lattice distortion represented by a very small displacement δr. The new hopping $t'(r_i + \delta r)$ can be expanded as

$$t'(r_i + \delta r) \approx t'_0 + \alpha \cdot \delta r, \tag{4.6}$$

where α is the slope of t': $\alpha = \frac{\delta t'}{\delta r}$, so the value of α is strongly dependent on the functional form of $t'(r)$ and the value of r_i. Notice, when the variation of the position of the top site is relatively small, the change of the hopping parameter can be well approximated by a linear function. By adjusting the value of α and range of δr, we can easily model a 9% gap variation.

The variation of the apical site can be the displacement along vertical and horizontal directions. A vertical displacement δh is equivalent to the case discussed in the Sec. 4.3.1 except for converting the dependence of the hopping parameters to that of a spatial displacement. Because $\delta h \approx \frac{r_0}{h}\delta r$,

$$t'(h + \delta h) = t'_0 - A \cdot \delta h, \tag{4.7}$$

where $A = \alpha \cdot \frac{r_0}{h} = \frac{\delta t'}{\delta h}$. A is the gradient of hopping t' along the vertical (z) direction. The pairing gap can be calculated as a function of the vertical displacement based on Eq. (4.7). The horizontal displacements seem more complicated because

it involve x and y two directions, but actually because of the linearity on both directions, the amount of changes in x and y directions can be equivalently added to the z direction as if there is only movement on vertical direction. Therefore, we can ignore the movement along the horizontal directions and only use the result from vertical displacement δh.

We choose t' to be 0.34 and confine the change of the position of apical site $|\delta h| < 0.002a$. Fig. 4.3 plots the charge of gap Δ^c as a function of δh at different A values. In order to simulate the sinusoidal gap behavior, we consider $\Delta^c(\delta h)$ as a linear function of δh. The plots in Fig. 4.3 show two regions with different slopes, but only in the region with higher slope, the apical atom is close enough to interact with the basal electronic pairing states. Therefore the useful region for our simulation is only confined to a small region of displacement δh. As discussed in Appendix 4.3.4, we need to have the range of the linear function smaller than $|\delta h = 0.001|$ in the simulation. According to Fig. 4.3, at $A = 0.5$, the linear range with higher slope up to (approximately) $\delta h = 0.001$ achieves an amplitude of about 10% of the equilibrium gap magnitude, which is close to the experimental result (9%), so $A < 0.5$ is probably the suitable region for A in the simulation.

4.3.3 Pairing modulation

In this section, we show the results of numerical calculations of pairing gap variation within individual unit cells for various displacements of the apical sites on su-

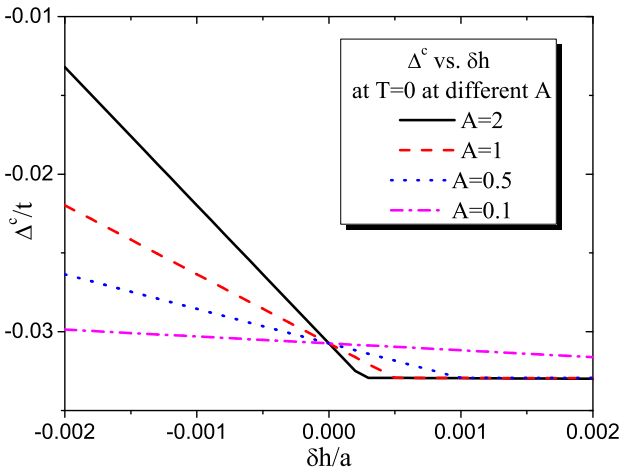

Fig. 4.3: The charge gap Δ^c is plotted as a function of the vertical displacement of the apical site from its equilibrium position at various A values (A is the gradient of hopping t' on the vertical direction). The hopping parameter between apex and base at the equilibrium position is $t'_0 = 0.34t$. The plot shows two regions with different linear slopes. The apical site should be close enough to the base so that it can provide sufficient sufficient effect on the electronic state on the base. In the figure, this requires δh to have a large slope. As A increases, the linear regime with higher becomes smaller. For $A = 0.5$, the linear range with higher slope up to about $\delta h = 0.001$ yields a modulation amplitude of about 10% of the gap at equilibrium position which means that $A < 0.5$ is the suitable region for the simulation.

perconducting pairing. The gap modulation has been found in $Bi_2Sr_2CaCu_2O_{8+\delta}$ using scanning tunneling microscopy is found to follow the supermodulation of the lattice structure. We apply our exact results on the square pyramids near the optimal $U = 3$ values to fit into the data for the experimentally observed variation of gap with the unit cell distortions.

We study the impact of the apical atom on pairing by monitoring the (locally) pairing gap as a function of the vertical displacement δh of the apical vertex from its average position. Experiments have shown that the modulation of the lattice structure can be expressed as a sinusoidal function with respect to a phase ϕ which is defined according to the period of the supermodulation [68]. To simulate this modulation, we introduce a sinusoidal modulation of the apical site along the vertical direction: $h(\phi) = h_0 + \delta h \cdot \sin(\phi + \delta)$, where h_0 is the equilibrium position of the apical site and the hopping between the apex and the base is set to $0.34t$. ϕ here is a phase according to the period of the modulation of the apical site and δ is a constant phase shift. We derive the pairing gap modulation $\Delta^P(\phi)$ as a function of ϕ. Using properly chosen parameters, we can fit our results to the experimental data of Slezak et al.([68]). The fitting along with the experimental observation corresponding to the sinusoidal behavior is shown in Fig. 4.4 under optimal doping. The details of the fitting procedure are given in Appendix 4.3.4. Our calculations are consistent with results in the Ref. [68] which shows a 9% modulation of average gap value for the optimally doped $Bi_2Sr_2CaCu_2O_{8+\delta}$. The

fitting parameters are $t = 1.53eV$ and $A = 0.35$. A, one of the free parameters, is within the range $0 < A < 0.5$ and hence it is consistent with our discussion in the Sec. 4.3.2. The value of t, which is the other free parameter, is close to values derived from other theoretical methods [77,78]. This provides additional evidence for the validity of our model.

4.3.4 Effects due to U_{apical}

One interesting question has to do with the intrinsic origin of this pairing gap modulation. We have examined this by monitoring the electron count at the apical site and the charge gap (Figure 4.5) as a function of the apical, on-site Coulomb interaction U_{apical}. In this modified Hamiltonian, all the basal sites were assigned the value $U = 3$ while U_{apical} is varied. From Fig. 4.5, it is evident that the negative gap region (i.e., pairing) occurs when the charge count at the apical site is approximately one electron. The above result indicates that the modulation effects observed and fitted to, which occur in the negative gap region, are strongly coherent phenomena where the electron count in the basal plane remains at four. The paired electrons in the plane do not couple that strongly to the apical site in this region. However, when U_{apical} approaches zero, the (negative) pairing gap is destroyed which can be explained as being due to the apical site allowing double occupation (hence pulling electrons from the basal plane). This simple picture can be used to roughly explain why the apical vacancies diminish

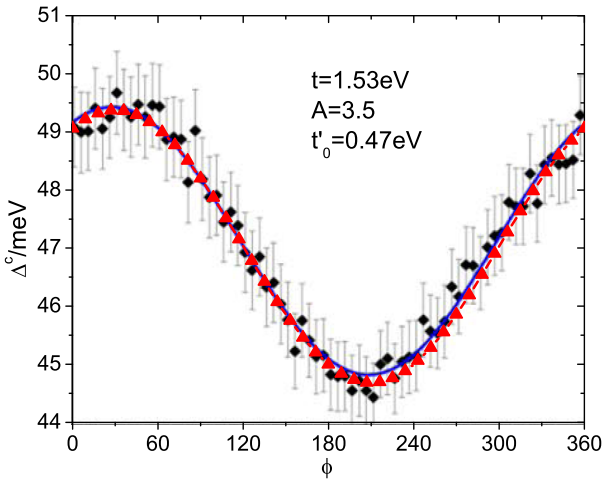

Fig. 4.4: Gap modulation due to lattice structure supermodulation where ϕ is defined as the phase of lattice structure supermodulation which can be expressed as a sinusoidal variation. The black diamonds with error bars are experimental data with uncertainties from Ref. [68]. The red triangles are fitted data from our model. The fitting gives the following parameters for modeling: $A = 0.35$, $t = 1.53eV$ and $t'_0 = 0.47eV$. Note that there is excellent agreement between experiment and the results from the other microscopic model. [77,78]

superconducting pairing as observed indirectly through pseudogap measrements as reported in Ref. [79].

The sinosudal modulations of the pairing gap are a direct result of rather small changes in the many electron spectrum with no level crossings. However, as the U_{apical} becomes very small or large, the apical site directly or indirectly changes the electron count in the plane, due to level crossings, thereby destroying the coherent pairing. This is a true many-body effect, driven by the many electron spectrum and level crossings associated with it, as a function of various parameters of the problem.

Details of fitting modulations

The experiment (see [68]) shows a cosinusoidal superconducting gap behavior. The average gap value at optimal doping is about 47meV and the (peak-to-peak) amplitude of gap modulation is about $9-10\%$ of the average gap value. The sinusoidal behavior is caused by the super modulation in the structure of the BSCCO system. The detail of the modulation structure can be found in Ref. [70]. From these papers, The CuO_2 layer does not change too much from the original square structure, but the SrO and BiO layers are strongly distorted. Therefore, the modulation is mainly coming from the changes of SrO and BiO layers and the modulation of the Bi and Sr atoms are found to be combination of sinusoidal

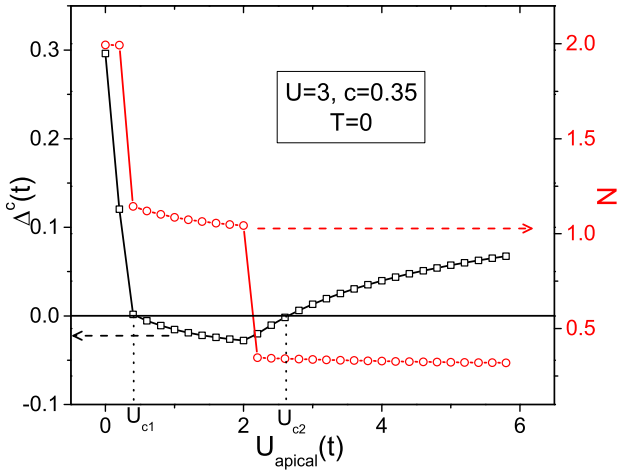

Fig. 4.5: Charge gap Δ^c (black squares) vs the onsite Coulomb interaction at the apical site U_{apical} while holding the basal $U = 3$. When U_{apical} is close to zero ($U_{apical} < U_{c1}$) or large enough ($U_{apical} > U_{c2}$), Δ^c is positive, indicating lack of pairing. Only when ($U_{c1} < U_{apical} < U_{c2}$, Δ^c is negative and pairing is favored. The pairing gap will be destroyed either by a too large U_{apical} or by a too small U_{apical}. Also shown is the average number of electrons on the apical apex N (red circles) corresponding to the above range of U_{apical} values. The value of N changes in steps. When $N = 2$, $\Delta^c > 0$ indicating no pairing since electrons are pulled away from the CuO_2 plane. When N is around 1, $\Delta^c < 0$. As N changes over to $N < 1$, Δ^c increases and eventually becomes positive. This suggests that the largest pairing gap appears at about $N = 1$; when N deviates from 1 the pairing gap becomes weaker and eventually disappears.

waves.

In our model, the effects of the SrO and BiO layers are included in the apical site of the pyramid Hubbard model. The distortion of the two layers can be simulated by the displacement of the apical site along vertical and horizontal direction. As mentioned in Sec. 4.3.2, only the vertical displacement is essential in our model due to the requirement of a strong square symmetry, so the horizontal distortions can be ignored. The equilibrium hopping term t_0 between top and base is set to $0.34t$ at which the pairing gap is about $0.30t$. In the experiment the average gap value is $0.47eV$, so $t = 1.53eV$. Experiments [68,70,80] shows that the vertical amplitudes of the modulation layers are about $0.01c - 0.02c$ where c is the vertical lattice constant. The amplitude of vertical displacement of the apical site in our model should be much smaller than experimental results because the simplified apical site averages, as a matter of fact, describe displacements of several (coupled) layers in real material. In the paper, we set the amplitude to $\delta h_max = 0.001$. The fitting with experimental results also provides $\alpha = 3.5$ and $\delta = \frac{\pi}{6}$ by the amplitude and the phase shift of gap modulation.

4.4 Summary

The effects of disorder in the position of the apical atom outside the CuO_2 plane on the superconducting gap have been investigated in $Bi_2Sr_2CaCu_2O_{8+\delta}$

($Bi-2212$) within the framework of small single band Hubbard clusters. We have shown that exact cluster calculations in appropriate geometries can quantitatively describe the displacements of the atoms in the bulk of $Bi_2Sr_2CaCu_2O_{8+\delta}$ material with its well-known supermodulation behavior. The theory provides strong evidence that the supermodulation is correlated with the out-of-plane displacement of the apical site and shows how variations of the inter-atomic distances affect the coupling and maximum of the superconducting energy gap.

These calculations can also be extended to finite temperatures, different doping levels or electron concentrations or can be applied to slightly different (octahedron, tetrahedron, etc.) geometries. The obvious next step is to see how the charge gap variations change with temperature and its relationship with the critical temperature T_c of the cuprate superconductors to explore methods of enhancing and maximizing T_c. In a nutshell, the properties from cluster studies of repulsive electrons contains the essential elements for understanding the variations of pairing gap and modulation in inhomogeneous, large systems. It can also help to understand the role of local out-of-plane impurities tied to the mechanisms of superconductivity in other layered high T_c superconductors.

Chapter 5

Electronic Nematicity in the square lattice

5.1 Introduction

When the calculations of isolated clusters suffer from the limited cluster size and complicated edge effects, some approximate computational methods extend quantum cluster calculations to the thermodynamic limit (infinite lattice). This is another option and such methods can provide support to the results of isolated clusters. In this thesis, the variational cluster approximation (VCA) is used (see Chapter 2) for the above purpose. We developed our own VCA code and the code has been tested by comparing its output with some published results in Refs. [47,81]. The first task undertaken is a study of electronic nematic orders.

The electronic nematic order is a phase discovered in recent measurements of magnetoresistivity, resistivity, IR reflectivity and neutron scattering in ruthenates [82], iron-based superconductors [83,84] and cuprates [85,17,86,87,18]. It locally

breaks the rotational point group symmetry (C_4) along the x and y axes (these directions for cuprates, defined along the Cu-O bond directions in the Cu-O plane) but preserves the translational symmetry. The symmetry of this phase greatly resembles the well-known nematic phase in isotropic liquid crystals, and hence the phase is called an electronic nematic state.

A two-dimensional (2D) electronic nematic phase is usually referred to as a phase that spontaneously breaks the symmetry of the underlying Hamiltonian associated with interchanging the x and y axes (defined in a certain plane) of the system [88]. Unlike conventional liquid crystals, in which the nematic state is due to the special shape of the molecules or the anisotropic interaction between molecules, the origin of an electronic nematic phase is the local electronic correlation. When the local C_4 symmetry is reduced to C_2 symmetry, the system is expected to have a 2-fold degenerate ground state. The two ground states will be randomly distributed on the 2d plane and will form locally different domains similar to magnetic domains in an Ising model. The effects of differently oriented domains are very likely to cancel out globally (i.e., on a larger length scale) and give rise to a lattice that appears uniform (i.e., without the above symmetry breaking).

It is technically difficult to detect the local electronic nematic symmetry breaking with disordered domains. Many experiments focus on $YBa_2Cu_3O_{6+x}$ because its orthorhombic structure plays a role similar to an external field that can

align nematic domains along the same direction, so that it is easy to measure the macroscopic anisotropic effect. However the orthorhombicity also makes it hard to distinguish whether the anisotropic effect is caused by the distorted lattice structure or the local electronic correlation. Recent publications [85,86] have reported a clear and strong anisotropic resistivity even when the orthorhombicity is well suppressed and the temperature dependence of the anisotropic effect is different from that of a lattice distortion. This implies that the in-plane transport anisotropy cannot be explained solely by distorted lattice structures. This result was later supported by a cellular dynamical mean field theory (CDMFT) [39] study of the two-dimensional Hubbard model by Okamoto *et al.* [89]. They showed that a strong nematic resistivity could be induced by a very small orthorhombic distortion as long as the interaction is strong enough to yield a Mott transition.

Another way to identify local nematicity is by using scanning tunneling spectroscopy (STS) with a rather high resolution. The STS can detect directly the electronic density of states within a nematic domain. In a recent publication, it is reported that the state-of-the-art STS measurements show "intra-unit-cell" electronic nematicity [18] on a perfectly symmetric lattice along the x and y axes *i.e.,* a lattice that is not orthorhombic. Thus, this measurement provides the most direct evidence that the local nematic effect, in some strongly correlated materials, is purely electronic and originates from repulsive electron-electron interactions.

The experimental results from STS detection depict a fascinating picture of

disordered local nematic states fluctuating throughout the undistorted cooper oxide plane, but, to our knowledge, there is no simple theoretical model supporting this idea. The motivation for this report is the possible existence of a ground state of the one-band Hubbard lattice Hamiltonian with spontaneous $x - y$ symmetry breaking. In order to identify and address such a locally nematic ground state, a real-space quantum cluster method [45] which can treat both the local and global effects at the same time is probably the best option for the problem. In this chapter, the variational cluster approximation (VCA) [41] calculations are performed on a C_4-symmetric, two-dimensional Hubbard square lattice. The results from the VCA calculations are used to make further analysis of this phase.

5.2 Reference System for Solving Nematicity

In order to deal with nematic broken symmetry, we have to introduce a fictitious field to represent the nematic order in the reference system like AF and SC orders discussed in Sec. 2.2.2. The smallest reference clusters: 2×2 (square symmetry) clusters are used for this chapter and let t' denote the hopping parameters in the reference system. The clusters use open boundary conditions according to Ref. [41] and t' is one of the variational parameters for the VCA calculation. Actually, one can also apply the larger-sized Betts clusters to reduce the size and edge effects [52,90].

The fictitious field is defined as following: the nematic state gives rise to a

fictitious difference between hopping along x and y directions; this difference can be addressed by introducing an additional term

$$H_\delta \equiv \delta \sum_{\boldsymbol{r}} t'(\hat{c}^+_{\boldsymbol{r}} \hat{c}_{\boldsymbol{r}+x} - \hat{c}^+_{\boldsymbol{r}} \hat{c}_{\boldsymbol{r}+y}) + H.c. \tag{5.1}$$

where δ denotes the fictitious deviation of the reference system from C_4 symmetry. The subscript $\boldsymbol{r}+x/\boldsymbol{r}+y$ indicates the nearest neighboring site along the x/y direction in the reference system. Here, we confine ourselves to $\delta > 0$, which means that the hopping along the x direction of the reference system is larger or equal to that along the y direction. This will provide one ground state, and because the ground state for nematic order is two-fold degenerate, the other ground state is symmetric to the first ground state with a larger hopping along the y direction. The AF order, Weiss field M (See Sec. 2.2.2), is also included in the variational calculation. It is important to note that M and δ are both fictitious parameters, which indicate the influence of long-range order on the small clusters, so the bigger the size of the cluster, the smaller the fictitious parameters are. This rule can be used to justify the validity of the fictitious parameters: the case for M is proved following this rule in Ref. [81].

Finally, with these one-particle variational parameters, the reference system

is represented by a Hamiltonian $\hat{H}'$ given by

$$\begin{aligned}\hat{H}' = \sum_{\langle \boldsymbol{r},\boldsymbol{r}'\rangle\sigma} & - (t'\hat{c}^{+}_{\boldsymbol{r}\sigma}\ \hat{c}_{\boldsymbol{r}'\sigma} + H.c.) - \mu' \sum_{\boldsymbol{r}} \hat{n} \\ & +\delta \sum_{\boldsymbol{r}} [t'(\hat{c}^{+}_{\boldsymbol{r}}\hat{c}_{\boldsymbol{r}+x} - \hat{c}^{+}_{\boldsymbol{r}}\hat{c}_{\boldsymbol{r}+y}) + H.c.] \\ & +M \sum_{\boldsymbol{r}} e^{i\boldsymbol{Q}_{AF}\cdot\boldsymbol{R}}(\hat{n}_{\boldsymbol{r}\uparrow} - \hat{n}_{\boldsymbol{r}\downarrow}) + U \sum_{\boldsymbol{r}} \hat{n}_{\boldsymbol{r}\uparrow}\hat{n}_{\boldsymbol{r}\downarrow} \end{aligned} \tag{5.2}$$

where $\hat{H}'$ contains the same interacting term as $\hat{H}_I$ in Eq. 1.2. A series of trial self-energies are determined from a variational calculation which finds out the stationary points (which can be maxima, minima or saddle points) of the self-energy functional $\Omega[\boldsymbol{\Sigma}]$.

The variational calculation involves four variational parameters (t', μ', M and δ) making it difficult to find the correct stationary point(s), because it is not possible to search every corner of the variational space completely. Therefore, we carry out the search in this report as follows: (1) set $\delta = 0$ and $M = 0$ to find a trivial solution by the VCA; (2) vary only the fictitious deviation δ and the effective Weiss field parameter M while fixing all the other parameters from the previous process; (3) as long as a non-trivial result ($\delta \neq 0$ or $M \neq 0$) shows up, an additional variational process with all the variational parameters will be performed to get the final result. The above three-step process is the most efficient way we have found in order to obtain a consistent variational behavior within the limited computer resources and time. We use a VCA program written by ourselves in FORTRAN. The program has been tested extensively and verified with results

in some published work such as Refs. [41,46,81].

5.3 results

5.3.1 Existence of local nematicity

The most important question is whether a local nematic state really exists in our simple model. The general experience from VCA calculations is that as long as the second step of the variational process mentioned in Sec. 2 gives a nontrivial result, the true stationary point obtained in the third step is very likely to be nearby and the nontrivial result usually survives in the third step. Therefore, we can use results from the second step to testify the validity of the model.

The dependence of the grand potential Ω on the fictitious deviation $\delta = |t_x - t_y|/(t_x + t_y)$ is calculated at different chemical potentials μ which determines the average electron density of the lattice by the thermodynamical equation: $\langle n \rangle = -\frac{1}{N}\frac{\partial \Omega}{\partial \mu}$. Fig. 5.1 is a plot of the difference $\Omega(\delta) - \Omega(\delta = 0)$ as a function of δ at $U = 4$ and $T = 0$ for $\mu = 2.0$ and $\mu = 1.36$. Notice that parameter δ can be varied only within the interval [0,1]. There are several stationary points in the two plots but, generally, the lowest point is usually the best guess for the proper stationary point representing physical properties. The red arrows mark the proper

stationary points in both cases respectively. At $\mu = 2.0$ (half-filling), the proper stationary point is at $\delta = 0$ implying that a uniform self-energy is preferred, while at $\mu = 1.36$ (far below half-filling), a non-zero fictitious deviation shows up which elucidates the possibility of a local nematic state. Although it is not the exact stationary point of the whole variational space because other variational parameters are fixed, usually the true stationary point is not too far away, so the ground state at the true stationary point is very likely to remain nematic.

We also use 2×3 clusters as our reference system to justify the results related to nematicity. Fig. 5.2 shows a nonzero stationary point which demonstrates the existence of a local nematic state within this reference system. The fictitious deviation δ within this reference is smaller than that within the 2×2 reference system. As discussed in previous sections, δ is a parameter expected to indicate the residual effect of nematic symmetry breaking from other parts of the whole lattice, so the larger the cluster, the smaller the residual effect, *i.e.,* smaller δ. Therefore, δ is expected to be smaller in 2×3 clusters calculation.

5.3.2 Antiferromagnetism and locally nematic state

There are many competing phases in strongly correlated materials; whether two phases can coexist is also an issue very much tied to the correlations of these phases. We have tested the possibility of coexistence of the AF phase and the

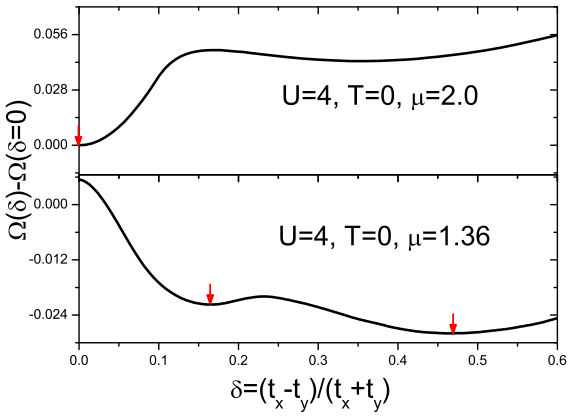

Fig. 5.1: Dependence of the grand potential Ω on the fictitious deviation $\delta = |t_x - t_y|/(t_x + t_y)$ is obtained from VCA calculation (the difference $\Omega(\delta) - \Omega(\delta = 0)$ is plotted) on an infinite square lattice tiled by 2×2 clusters (see Fig. 2.2). The on-site Coulomb interaction is $U = 4$ and temperature is $T = 0$. The energy unit is given by the nearest neighbor hopping of the original lattice. The upper figure is calculated when chemical potential $\mu = 2.00$ (half-filling). The non distorted stationary point with $\delta = 0$ implies that there is no nematicity for half-filling ground state. In contrast, the lower plot at $\mu = 1.36$ (off half-filling, $n \approx 0.76$) has two stationary points with $\delta \neq 0$ shown by red arrows: one at $\delta = 0.16$ and the other at $\delta = 0.47$. After further optimizations with other variational parameters, only $\delta = 0.47$ remains as the ground state which points to the local nematicity.

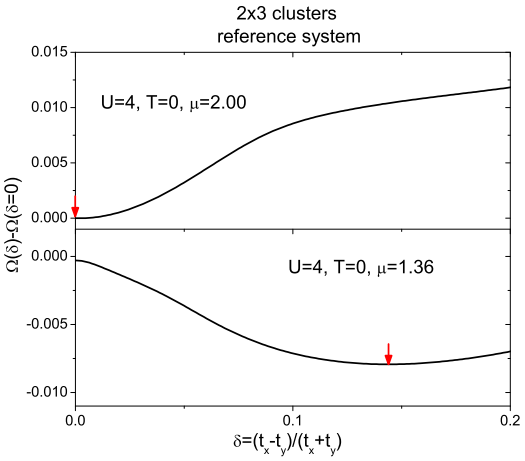

Fig. 5.2: 2×3 clusters are used as the reference system. The fictitious deviation $\delta = |t_x - t_y|/(t_x + t_y)$ is obtained from VCA calculation. The difference $\Omega(\delta) - \Omega(\delta = 0)$ is shown at $\mu = 2.0$ ($n = 1.00$) and $\mu = 1.36$ ($n \approx 0.76$). A non-zero stationary point at $\delta = 0.14$ is found at $\mu = 1.36$. This shows the stability of the local nematic ground state in the pseudogap region at sufficient doping $n \approx 0.76$.

nematic state. In order to study the AF ground state, an effective (static) AF Weiss field M is introduced in the reference system to include AF broken symmetry in the trial self-energy space, and we emphasize that the AF order is a static order and has the simplest form with a AF vector $\boldsymbol{Q}_{AF} = (\pi, \pi)$ (see Sec. 2).

After searching for possible stationary points in the variational space consisting of both nematic and AF phases, the fictitious deviation δ and the AF Weiss field M are calculated simultaneously for different electron densities n and the results are plotted in Fig. 5.3. In the plot, when one variational parameter is nonzero, the other one turns out to be zero. This result shows that the proper physical state of this simple Hubbard model cannot support the coexistence of static AF order and nematicity, i.e., static AF order with an AF vector $Q_{AF} = (\pi, \pi)$ cannot simultaneously break the local C_4 symmetry. However this conclusion is not applicable to other forms of AF orders. In fact, experiments have shown that the nematicity can exist in the pseudogap region [88], where some local magnetism is still retained. The reason we did not see such coexistence is probably due to the fact that the static AF order with $Q_{AF} = (\pi, \pi)$ requires an electronic structure with a perfect C_4 symmetry, while the nematic state breaks that symmetry. It is possible that the AF state coexists with local nematicity when it is not static or has a differently oriented AF vector. For example, a spin density wave phase or $Q_{AF} = (\pi/2, 0)$, because this kind of AF phase does not strictly require C_4 symmetry, the two phases may have a chance to coexist.

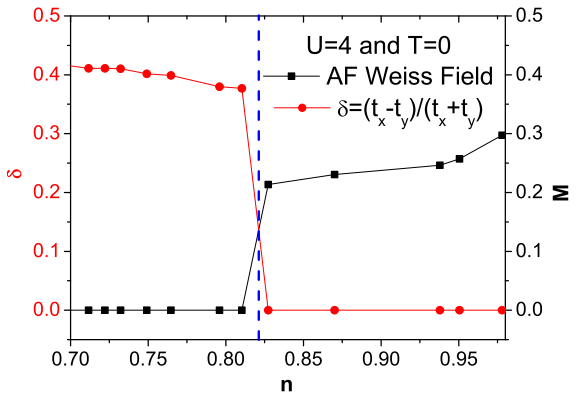

Fig. 5.3: The fictitious deviation δ and AF Weiss field M are plotted simultaneously as a function of the electron density n at $U = 4$ and $T = 0$. When $\delta \neq 0$, M is zero and when $M \neq 0$, δ is always zero. This plot indicates that the AF phase with $Q_{AF} = (\pi, \pi)$ and the local nematic state cannot coexist.

5.3.3 Strongly correlated case

In order to study the case with strong electronic interactions, we study $U = 8$ case for the model. The fictitious deviation δ at different electronic densities n for $U = 4$ and $U = 8$ are plotted in Fig. 5.4. At $U = 4$, the nematic state can exist from the overdoped region to the optimally doped region. The value of δ decreases with increasing electronic density, which implies that the nematicity is suppressed by local magnetic orders which begin to form as the electronic density becomes larger. At $U = 8$, δ behaves the same as that at $U = 4$ in the overdoped region. However, around optimal doping, δ jumps to about $\delta \approx 1$ at $U = 8$. This abnormal behavior at $U = 8$ points to a picture where the local hopping in one direction becomes close to zero, which suggests that the two-dimensional lattice is reduced to quasi one-dimensional chains. This strong coupling phenomenon is very similar to the stripe phase with charge and spin modulations coupled with broken rotational and translational symmetries found in some strongly correlated high T_c superconducting materials. Such a strong trend to form inhomogeneous pattern of holes and spins is often referred to as charge and spin phase separation instabilities. The same abnormality was also reported by Okamoto *et al.* [89], and they have given similar explanations. In our opinion, the stripe phase simultaneously breaks rotational symmetry and translational symmetry, but our model does not examine the broken translational symmetry. Therefore, it is not clear

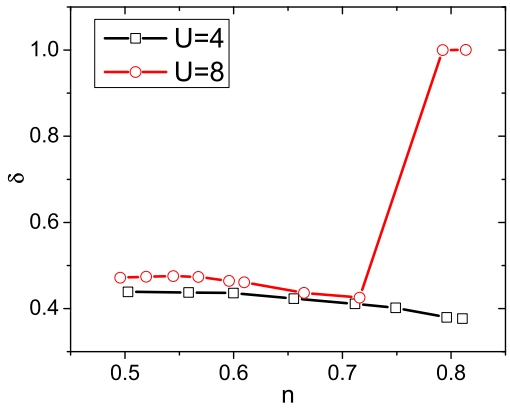

Fig. 5.4: The fictitious deviation $\delta = |t_x - t_y|/(t_x + t_y)$ from VCA calculation is plotted as a function of electronic density n for $U = 4$ and 8. For $U = 4$ (open square), δ is decreasing with electronic density up to $n < 0.8$. For $U = 8$ (open circle), δ behaves the same as $U = 4$ case within the overdoped region but increases up to nearly equal to one around optimal doping at $U = 8$, which is probably a signal of transforming into the stripe phase.

whether this abnormal behavior signals the transformation into a stripe phase or just a "spurious" solution (with no physical content).

5.3.4 Order parameter of local nematicity

As for local order, important insights can be obtained by examining a lo-

cal order parameter. For example, STS experimental work by Lawler et al. [18] measured the local density of state (LDOS) within each "sub-unit-cell" with a very high real-space resolution, which helped them to successfully identify the local nematicity. They defined a real-space order parameter to quantify real-space nematicity based on the LDOS on different atoms.

In order to identify the local nematic state in the two-dimensional Hubbard model, we define the nematic order parameter based on the local correlation function at different transition energy. The local correlation function ρ is defined as

$$\rho(\boldsymbol{r},\omega) = \langle \hat{S}^z(\boldsymbol{r},\omega)\hat{S}^z(\boldsymbol{r}',\omega)\rangle \tag{5.3}$$

where $\hat{S}^z(\boldsymbol{r},\omega)$ is the spin operator at position $\boldsymbol{r}$ and energy ω. $\boldsymbol{r}$ and $\boldsymbol{r}'$ are the nearest neighbors either along x direction ($\boldsymbol{r}' = \boldsymbol{r} + \hat{x}$) or along y direction ($\boldsymbol{r}' = \boldsymbol{r} + \hat{y}$). Therefore, the nematic order O which breaks the C_4 rotational symmetry can be defined as

$$O(\boldsymbol{r},\omega) = \frac{\langle \hat{S}^z(\boldsymbol{r},\omega)\hat{S}^z(\boldsymbol{r}+\hat{x},\omega) - \hat{S}^z(\boldsymbol{r},\omega)\hat{S}^z(\boldsymbol{r}+\hat{y},\omega)\rangle}{\langle \hat{S}^z(\boldsymbol{r},\omega)\hat{S}^z(\boldsymbol{r}+\hat{x},\omega) + \hat{S}^z(\boldsymbol{r},\omega)\hat{S}^z(\boldsymbol{r}+\hat{y},\omega)\rangle}$$

In the normal state, because of C_4 symmetry, the local correlation functions along x and y will be always zero. For a local nematic state, the local correlation functions along x and y directions will not be the same. Therefore, $O(\omega)$ is zero in the normal state and nonzero in the local nematic state. The nematic fluctuations in the uniform Hamiltonian can exist locally within each "sub-unit-cell". In general,

the local order parameter and correlation function both depend strongly on the number of momentum channels that are counted in our calculations.

Fig. 5.5(a) shows a comparison between local order parameters at two different electronic densities. The local nematicity shows up at $n = 0.81$. When $O(\omega)$ is not zero, *i.e.,* in the local nematic phase, we further evaluated the summation of local density of state along x and y directions (not shown) and found them the same along the x and y direction. This factor suggests that the lattice structure at local nematic phase still has C_4 symmetry, which provides an evidence that the nematic order is caused only by a local effect. This kind of local order can probably be considered as being due to a modification of the shape of local $d_{x^2-y^2}$ orbitals. The orbitals energetically prefer to elongate along one direction and, at the same time, shorten along the other direction, and this process is fluctuating throughout the whole lattice while the center of the orbital (*i.e.,* the position of the Cu atom) maintains translational symmetry. With different electronic density n, the local order parameter O is calculated at zero transition energy in Fig. 5.5(b). The local order parameter is increasing as the electronic density increases. This trend is probably showing that the electron correlations play an important role in the nematic phase, since electron correlations are enhanced when electronic density grows.

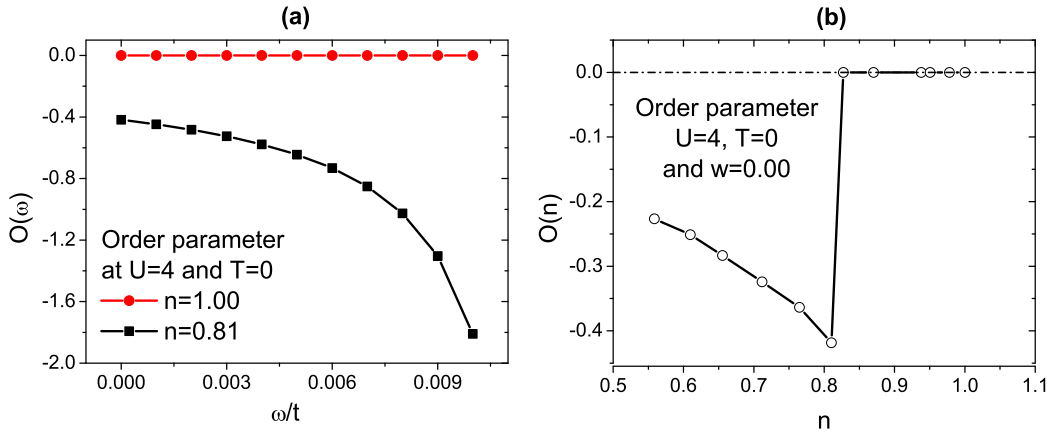

Fig. 5.5: (a) Local nematic order parameter O is plotted as a function of energy ω at $U = 4$ and $T = 0$. The result is obtained by summing up 10×10 momentum $\boldsymbol{k}$ points in the reciprocal lattice. The circles denote the order parameter at electron density $n = 1.0$ (half-filling) and the squares represent the order parameter at electron density $n = 0.8$. The magnitude of O at $n = 1.0$ is zero at all ω, which implies the non-existence of a nematic state. In contrast, O at $n = 0.81$ is non-zero for all ω showing local nematicity. (b) O is plotted as a function of electronic density n at $U = 4$ and $T = 0$ with a transition energy $\omega = 0$. In the nematic phase, O is increasing as electronic density increases.

5.3.5 Dynamical structure factor

Magnetic neutron scattering is a very useful tool to investigate magnetic and density fluctuations of a given material. In the simple one-orbital Hubbard model (Eqn. 4.1), spins can only be up or down, which means that we can only deal with spins S_z along a longitudinal direction, so that we can only examine the spin and density correlations of the longitudinal spins. Hence we define longitudinal spin correlation functions in real $S(\boldsymbol{r}_i, \boldsymbol{r}_j, t)$ and momentum space $S(\boldsymbol{k}, \omega)$ as follows:

$$S(\boldsymbol{r}_i, \boldsymbol{r}_j, t) = \langle S^z(\boldsymbol{r}_i, t) S^z(\boldsymbol{r}_j, 0)\rangle - \langle S^z(\boldsymbol{r}_i, t)\rangle\langle S^z(\boldsymbol{r}_j, 0)\rangle \tag{5.4}$$

$$S(\boldsymbol{k}, \omega) = \frac{1}{N}\sum_{i,j}\frac{1}{2\pi}\int_{-\infty}^{+\infty} dt e^{-i[\boldsymbol{k}(\boldsymbol{r}_j - \boldsymbol{r}_i) - \omega t]} S(\boldsymbol{r}_i, \boldsymbol{r}_j, t) \tag{5.5}$$

The real-space longitudinal spin correlation function is expressible as

$$S(\boldsymbol{r}_i, \boldsymbol{r}_j, t) = \sum_{\alpha} G_\alpha(\boldsymbol{r}_j, \boldsymbol{r}_i, -t) G_\alpha(\boldsymbol{r}_i, \boldsymbol{r}_j, t) \tag{5.6}$$

where G_α is the real-space-time Green's function and α is the spin index (up or down). The equation is the same as the result of density correlation function. Its Fourier transform is the so-called dynamical structure factor (DSF) which can be measured by neutron scattering experiments. Because we perform most of the calculations within the cluster framework, the DSF is finally written using cluster parameters defined in Fig. 2.2 as

$$\begin{aligned} S(\boldsymbol{k}, \omega) &= \int \frac{d\nu}{2\pi}\frac{1}{N}\sum_{RBZ} e^{-i\tilde{\boldsymbol{q}}\boldsymbol{X}_{ij}} \sum_{\boldsymbol{X}_{ij},\alpha} G_\alpha(\boldsymbol{X}_{ji}, \tilde{\boldsymbol{q}}, \nu) \\ &\quad \times G_\alpha(\boldsymbol{X}_{ij}, \boldsymbol{k} + \tilde{\boldsymbol{q}} - \boldsymbol{Q}, \nu + \omega) \end{aligned} \tag{5.7}$$

where $\boldsymbol{X}_{ij}$ is a lattice vector between the cluster sites i and j; $\boldsymbol{k}$, $\tilde{\boldsymbol{q}}$ and $\boldsymbol{Q}$ are reciprocal lattice vectors as defined in the caption of Fig. 2.2. G is the Green's function in the cluster representation; N denotes the number of sites in the lattice. The DSF represented by Eq. 5.7 involves coupling between two quasi-particles at $\tilde{\boldsymbol{q}}+\boldsymbol{k}$ and $\tilde{\boldsymbol{q}}'$ with energy $\omega+\nu$ and ν' respectively in $(\tilde{\boldsymbol{k}}, \omega)$ space. The correlation spectrum is not zero only when $\tilde{\boldsymbol{q}}+\boldsymbol{k} = \tilde{\boldsymbol{q}}'+\boldsymbol{Q}$ and $\omega+\nu = \nu'$ are both satisfied, *i.e.,* $\nu(\boldsymbol{k}+\tilde{\boldsymbol{q}}) - \nu(\tilde{\boldsymbol{q}}) = \omega$. This condition corresponds to an electron-hole excitation, which is only valid around the Fermi surface ($\tilde{\boldsymbol{k}_F}$) of the cluster superlattice.

The DSF density spectra for magnetic excitations is calculated around $(0, 0)$ in the momentum space at different energies. Fig. 5.6 shows a slice cut of the DSF spectrum along $(k_x, 0)$ and $(0, k_y)$. The large differences of the spectrum along x and y directions clearly show the asymmetry of the momentum-space density correlation function. This confirms that although the nematic state is a local effect in real-space, it still has a strong influence on some properties within the momentum space, especially on the two-particle correlations. We note that the stronger correlation switches from y direction to x direction as the excitation energy goes from very low to very high values as shown in Fig. 5.6. This means that there must be a "switching point" energy where the correlation along the x and y directions is symmetric, and we find that this point about $\omega \approx 0.05$. Therefore, the asymmetry of the correlation pattern around $(0, 0)$ decreases to zero and then increases again as the excitation energy increases. We cannot calculate

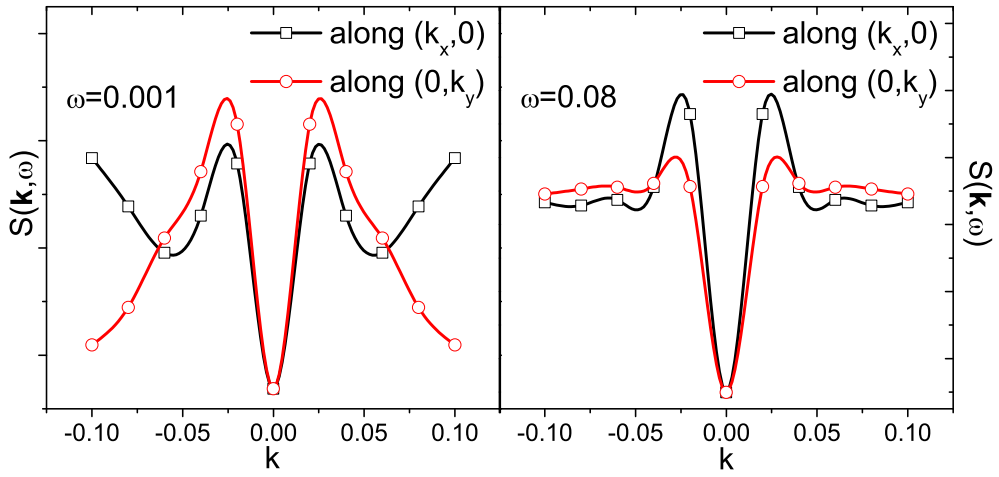

Fig. 5.6: The slice cut of the dynamical structure factor along $(k_x, 0)$ and $(0, k_y)$ at $U = 4$ and $T = 0$. This result is obtained by summing up 20×20 momentum space points and integrating over the energy window from -1.0 to 1.0. The results shown here are at two different energies $\omega = 0.001$ and $\omega = 0.08$. Both plots show large differences along the x and y directions, which elucidates that the nematic properties can show up at both low and high energy excitations. At low energy $\omega = 0.001$, the spectrum along the y direction is stronger but at high energy $\omega = 0.08$, the spectrum along the x direction becomes stronger.

the full (three-dimensional) spin correlation function because of the restrictions of the Hubbard model, but we have already seen some asymmetric properties in spin correlations, at least along the longitudinal directions. Therefore, the full spin correlation function should also show an asymmetric pattern along the x and y directions.

Although the magnetic neutron scattering work of Ref. [17] mapped nematic patterns of spin correlations at different incident energies, they also found that the nematic pattern disappears at high temperature and high incident neutron energy. The high temperature involves thermal effects that sample more and more normal state in the lattice with increasing temperature and eventually destroys the nematic pattern. Regarding high incident neutron energy, we did not see this trend in our results, at least for $\omega = 0.08$, our result does not show any sign that the nematicity becomes weaker. This mismatch with the neutron experiment can be explained simply by the following two reasons. Firstly, our calculations are applied only to the nematic ground state without the system being excited into the normal state possibly observed in the neutron scattering experiments. Secondly, it is possible that the incident neutron energy in the experiment is lower than the "switching point" energy. In this case, our obtained intrinsic energy spectrum also becomes more symmetric at higher energy which is consistent with this neutron experiment.

5.4 Summary

In conclusion, we have identified a local nematic phase away from half filling (in the overdoped region) by using the variational cluster approach to solve the one-orbital, two-dimensional Hubbard model. However, we do not find any coexistence of antiferromagnetic order and nematicity for their distinct symmetries. The variational cluster approximation shows evidence for electronic nematicity of the states close to the pseudogap energy consistent with the scanning tunnelling (spectroscopic-imaging) microscope measurements of the intra-unit-cell states in underdoped $Bi_2Sr_2CaCu_2O_{8+\delta}$ [18]. The breaking of rotational symmetry by the electronic structure within each CuO_2 unit cell becomes predominant in the pseudogap phase as the density of doped holes is reduced. Our results directly demonstrate that the nematicity can arise within a single orbital isotropic (non-degenerate) Hubbard model. The nematic phase is suppressed as the electron density increases toward the half filled state, but as electron density is close to optimal doping, while the Coulomb interaction is large enough, the nematicity suddenly gets enhanced and is likely to become a phase similar to the stripe structure. The dynamical structure factor shows that the real-space local effects also influence the correlations in the momentum space and the asymmetry of the correlation pattern changes with different incident energies.

Chapter 6

Possible electronic phase separation in the square and honeycomb lattice

6.1 Introduction

In the last chapter of the thesis, we revisit the electronic inhomogeneity using the VCA method in order to get further insights into electronic inhomogeneities. We also investigate possible phase separation in both square and honeycomb lattices from half-filling to optimal doping. We explore the microscopic mechanism of electronic phase separation using the VCA method on a two-dimensional Hubbard lattice without any additional input of long-range orders.

Recent discoveries suggest that phase separation is likely to occur in the vicinity of a metal-insulator transition (MIT) [91–93]. In contrast to one-dimensional systems, the two-dimensional (2D) Hubbard model in both square and honeycomb lattices at half filling is expected to exhibit a Mott-Hubbard MIT at finite on-site

Coulomb interactions U in the paramagnetic phase at both zero and finite temperature [94–99]. In general, this transition at a finite U value might be an intrinsic property of the 2D Hubbard lattice [99].

Electronic phase separation describes an inhomogeneous distribution of electron densities in the lattice, *i.e.,* the states with different electron densities in equilibrium can simultaneously coexist in the lattice. According to phase transition dynamics, the chemical potentials μ of different states with electron densities n have to be the same in the system [100] at equilibrium. Therefore, if n can be obtained as a function of μ, a multivalued n at a certain μ values can be considered as clear evidence of an electronic phase separation instability.

6.2 Results

6.2.1 Phase separation in the square lattice

Metal-insulator transition (MIT) at half filling

As mentioned in Sec. 1, the MIT might be relevant to phase separations, so we study the MIT at half filling first. The one-dimensional Hubbard model leads to a smooth MIT at infinitesimal U values and the absence of phase separation at any U value. In two dimensions, our VCA calculations for the square and honeycomb geometries provide strong support for a smooth second order Mott-Hubbard MIT at half filling. We found that a finite Coulomb interaction $U = U_c > 0$ is needed to open an energy gap around the Fermi level in the one-particle excitation spectra

for both (square and honeycomb) lattices. The U value at the transition (U_c) can be approached from both sides of U_c, but since finding U_c is not the main focus in this work, we only locate an interval in which U_c falls. In the square lattice, the MIT transition takes place between $1 < U_c < 2$, while in the honeycomb lattice it happens between $2 < U_c < 3$. We would like to emphasize that since we do not include any long-range magnetic order (by adding Weiss field parameters to reference systems) in the VCA calculation, the results reflect intrinsic properties of the 2D Hubbard model in the absence of long-range AF order. The results are compatible with several other calculations that utilize different numerical methods [94–98].

Phase separation away from half filling

Phase separation, caused by electron instabilities under hole doping, leads to the coexistence of inhomogeneous, hole-rich and hole-poor regions. This phenomenon closely resembles phase separation instabilities observed in first order phase transitions. The coexisting states with different electron densities n share the same chemical potential μ. The n vs μ plots are obtained for the square lattice at different Coulomb interactions U from our VCA calculation in Fig.6.1. It is found that the plots for the square lattice show discontinuities where the dependence of n on the chemical potential μ is multivalued. This means that electronic phase separation occurs in the square lattice at the vicinity of these discontinuities which is

similar to the classic phase separation in a first order phase transition. For example, at $U = 4$, the discontinuity of the plot appears at μ around 1.25 and the value of n changes abruptly from 0.946 to 0.977. These two states have almost the same chemical potential and, therefore, they can coexist in the system. When the lattice has an average electron concentration between 0.946 and 0.977, the lattice system will become phase separated and behave as a mixture of hole-rich ($n = 0.946$) and hole-poor ($n = 0.977$) regions, which leads to spatial inhomogeneities.

As U becomes larger, the magnitude of the discontinuity in n also increases (see Fig. 6.1), which suggests that the electron interaction plays an important role in the electronic phase separation. In addition, since no long-range order term (for spontaneous symmetry breaking) has been added in the variational calculation, the ground state is driven purely by local electron correlations. Electronic phase separation occurs at some finite Coulomb interaction strength U_c, which is close to the MIT transition value at half-filling. This result suggests that the electronic phase separation in the square lattice is closely related to the Mott-Hubbard transition, so the electronic phase separation is likely to be driven by the on-site Coulomb interaction. Similar results were also reported in Ref. [29] using DCA.

There are questions related to the sizes of the AF or metallic domains when the system is phase separated. As discussed in Chapter 1, experiments show that the length scale of inhomogeneities has very large range. Theoretically, the length scale should be determined by the interaction strength and correlation length in

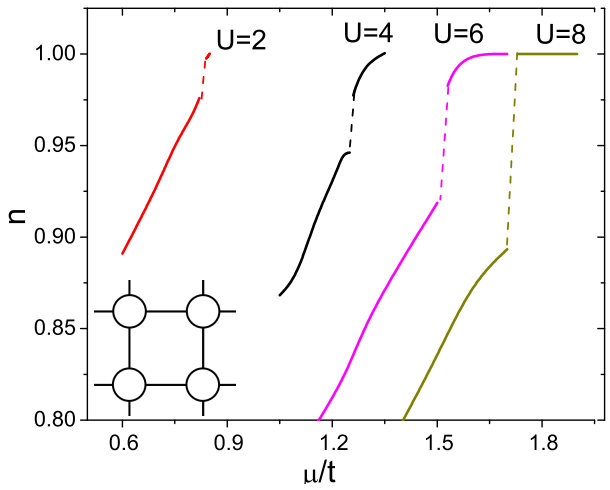

Fig. 6.1: The electron densities n as a function of chemical potential μ for the Hubbard model on a square lattice at different values of on-site Coulomb interaction U. The plots clearly show discontinuities at distinct n values in the square lattice for hole-doped case. The discontinuity means that states with different n at two edges of the step-like discontinuous transition have the same μ value, so they can coexist in the same system at the equilibrium, which creates a spatial variation of charge density in the material. The magnitude of the discontinuity of n becomes larger as U increases, which indicates that the phase separation is preferred when interaction gets stronger.

the model [22]. However, the correlations are restricted to the cluster size in the VCA and hence it is not possible to address this question directly from our calculation.

antiferromagnetic transition at phase separation

The similarity between this electronic phase separation found in the square lattice and the classic phase separation found in the first order phase transitions suggests that it is very likely that there is a phase transition when electronic phase separation happens. It is known that the lattice is antiferromagntic at half-filling and it becomes a metal with sufficient hole doping. The electronic phase separation found in the previous section may reflect a phase transition between the AF state and the metallic state. Although our VCA calculation does not include any long-range order for example the long range AF order, some AF orders may still appear locally at the cluster length scale because many-body effects are treated exactly at the cluster level in the VCA calculation. By analyzing the the transverse spin susceptibility χ, we confirm that there is an AF-normal transition when the system is electronically phase separated. χ is defined as

$$\chi_{ij}(\omega) = \int_0^\beta d\tau e^{i\omega\tau} \langle \hat{S}_i^+(\tau) \hat{S}_j^-(0) \rangle \tag{6.1}$$

with

$$\hat{S}_i^+(\tau) = \hat{c}_{i\uparrow}^+(\tau) c_{i\downarrow}(\tau)$$

$$\hat{S}_i^-(\tau) = \hat{c}_{i\downarrow}^+(\tau) c_{i\uparrow}(\tau)$$

When calculating $\boldsymbol{\chi}(\boldsymbol{k},\omega)$, we only count up to the zero-order diagram $\boldsymbol{\chi}^0(\boldsymbol{k},\omega)$ and ignore all the higher order terms which take into account the non-irreducible two-particle vertex $\Gamma(\boldsymbol{k},\omega)$. Although $\Gamma(\boldsymbol{k},\omega)$ contains important information about dynamical correlations, the $\boldsymbol{\chi}^0(\boldsymbol{k},\omega)$ is sufficient to be a "fingerprint" of a simple static AF local order with an AF vector $\boldsymbol{Q} = (\pi,\pi)$. Therefore, the transverse spin susceptibility in momentum space can be obtained from one-particle Green's function $\boldsymbol{G}(\boldsymbol{X};\boldsymbol{k},\omega)$ calculated by the VCA method as

$$\boldsymbol{\chi}(\boldsymbol{k},\omega) \approx \boldsymbol{\chi}^0(\boldsymbol{k},\omega) = \frac{1}{N}\sum_{\boldsymbol{q}}\int \frac{d\nu}{2\pi}\boldsymbol{G}_{\uparrow\uparrow}(\boldsymbol{X}';\boldsymbol{k}+\boldsymbol{q},\omega+\nu)\boldsymbol{G}_{\downarrow\downarrow}(\boldsymbol{X};\boldsymbol{q},\nu) \qquad (6.2)$$

where $\boldsymbol{X}$ in the one-particle Green's function denotes a real space vector between two cluster sites and N is number of $\boldsymbol{k}$-points that is used in the calculation.

We compare χ around the (π,π) point in the k-space for different electron concentrations. The results for $U = 4$ are plotted in Fig. 6.2 at half-filling ($n = 1$) and the two states right before and after phase separation ($n = 0.977$ and $n = 0.946$). At half-filling, there is a high susceptibility at the (π,π) point, which indicates a strong (saturated) AF correlation. At $n = 0.977$, there is still a small peak, so a relatively weaker AF order still exists at this concentration. While the system goes through the phase separation region, the AF correlation is destroyed since no peak is seen at the (π,π) point. This plot clearly shows when the electron density drops from 0.977 to 0.946, the AF correlation vanishes.

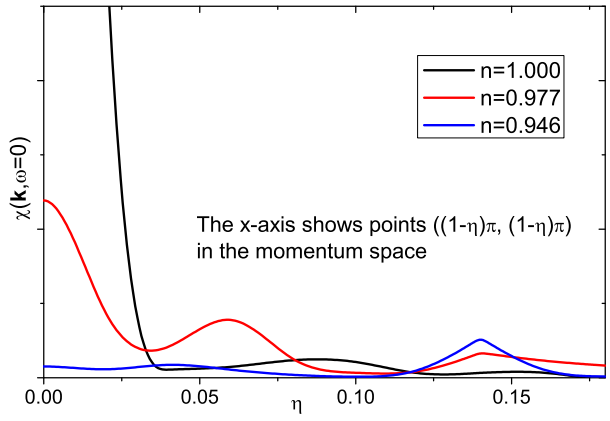

Fig. 6.2: The zero-frequency transverse spin susceptibilities $\chi(\boldsymbol{k}, \omega = 0)$ at $U = 4$ with different electron densities are obtained along (π, π)-$(0, 0)$ direction. The x-axis is denoting the $\boldsymbol{k}$ point at $((1 - \eta)\pi, (1 - \eta)\pi)$. $\chi(\boldsymbol{k}, \omega = 0)$ has a huge peak at (π, π) which is the "fingerprint" of a static local AF order. The peak remains but it is smaller when $n = 0.977$, which indicates that the local AF order can still be observed but it is not very strong. As the system goes through the phase separation region to a lower density ($n = 0.946$), the susceptibility peak disappears, so the AF correlation is totally destroyed.

Phase diagram of the square lattice

A hole concentration x vs. U phase diagram for the square lattice can be extracted from the above calculations as shown in Fig. 6.3. The metal (M), antiferromagnetic insulator (AFI) and phase separation (PS) are marked in the figure. This figure indicates that the square lattice has a phase separation region, in which the system is an inhomogeneous combination of a metal and an AF insulator. The range of change in the electron density at phase separation increases when U becomes larger, which indicates that the AF correlation plays an important role in generating the electronic phase separation.

Electronic properties at phase separation

In order to further study the electronic properties of Hubbard model at phase separation, we use the VCA-based one-particle (excitation) spectral function to help understand the physics of phase separation. The one-particle (excitation) spectral function $A(\boldsymbol{k}, \omega)$ is obtained from the one-particle Green's function $G(\boldsymbol{k}, \omega)$

$$A(\boldsymbol{k}, \omega) = -2 \lim_{\eta \to 0^+} \Im G(\boldsymbol{k}, \omega + i\eta) \tag{6.3}$$

where $\boldsymbol{k}$ is the k-point in the momentum space and ω is the real frequency. N denotes the number k-points that are counted in the VCA calculation. η is a small parameter referred to as the spectrum broadening factor and it is set to 0.015 throughout the calculation. We extracted the spectral function for the two densities right before and after the electronic phase separation. The single particle

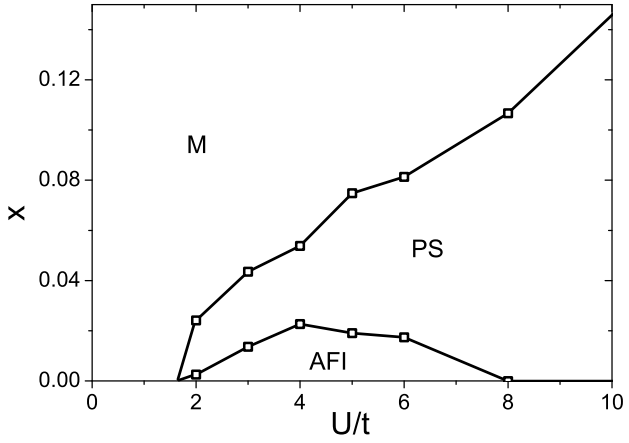

Fig. 6.3: Phase diagram of the Hubbard model in the square lattice. The phase diagram is drawn in the space of Coulomb interaction U vs. hole concentration $x = 1 - n$. In the figure, M stands for metallic phase, which exists when U is relatively low or the doping level is high. The AFI denotes antiferromagnetic insulator, which exists at moderate U values and low doping. PS is the phase separation region where AFI and M states are mixed and distributed inhomogeneously in the lattice.

excitation spectra at $n = 0.977$ and $n = 0.946$ with $U = 4$ are shown in Fig. 6.4. By comparing the spectral functions at the above two densities, one can find that a set of narrow spectra (enclosed by a blue rectangle in Fig. 6.4) around the Fermi level disappears when the electron density drops from 0.977 to 0.946, *i.e.*, this part of spectra at the Fermi level shows up in the AF state but disappears in the metallic state. This means that there is an instability of Fermi surface as phase separation occurs.

The part of spectra shown in Fig. 6.4 is narrow. The narrow band suggests the presence of relatively strong effective Coulomb interactions and hence electrons need extra energy to stay with other electrons in the state. The energy of the system is expected to increase when it approaches half-filling because more electrons are introduced to the narrow state. However, the local AF correlations also appear near half-filling which create a stable local magnetic structure which tends to decrease the total free energy of the system. These two competing effects (strong interactions and local AF correlations) give rise to an interesting situation: when the state is a mixture of a nearly half-filled state and an almost empty state, the total free energy is lower than a partially filled state with the same electron concentration. Therefore, the system energetically prefers redistributing over the lattice to form spatial charge variations, so that in some regions, the local electronic state is almost half-filled, while in other regions, the state is almost empty. This physical picture manifests the presence of a microscopic inhomo-

geneity, which achieves a lower total free energy than that of a uniform electron distribution.

This result is similar to what our group [24–28] has predicted using calculations for isolated Hubbard clusters. We have found, in bipartite Hubbard clusters, when a moderate on-site Coulomb interaction can make the energy of a mixture of electronic states of N electrons and $N-2$ electrons lower than that of a pure state with $N-1$ electrons, the system has a tendency to phase separate.

Another important point is that the position of this part of Fermi surface in the momentum space is the $(\pi/2, \pi/2)$ point (see the red arrow in Fig. 6.4 between the Γ point and M point and the red dots in Fig. 6.4(c)). Because the unit cell of the AF state contains two sites, the first Brillouin zone (FBZ) of the AF state is folded and the boundary of FBZ is from $(0, \pi/2)$ to $(\pi/2, 0)$. In the AF state, this part of Fermi surface resides on the FBZ boundary of the AF state. When the lattice becomes a metal, the unit cell only contains one site and the FBZ is unfolded (FBZ boundary deformation). The $(\pi/2, \pi/2)$ point is not on the FBZ boundary any more in the metallic state as shown in in Fig. 6.4(c). This part of Fermi surface at $(\pi/2, \pi/2)$ point also disappears. It seems the above Fermi surface instability is caused by the deformation of the FBZ boundary which is also related to the phase transition from an AF state to a metallic state. Similar conclusions were also predicted in Ref. [101,102] using the renormalization group (RG) method.

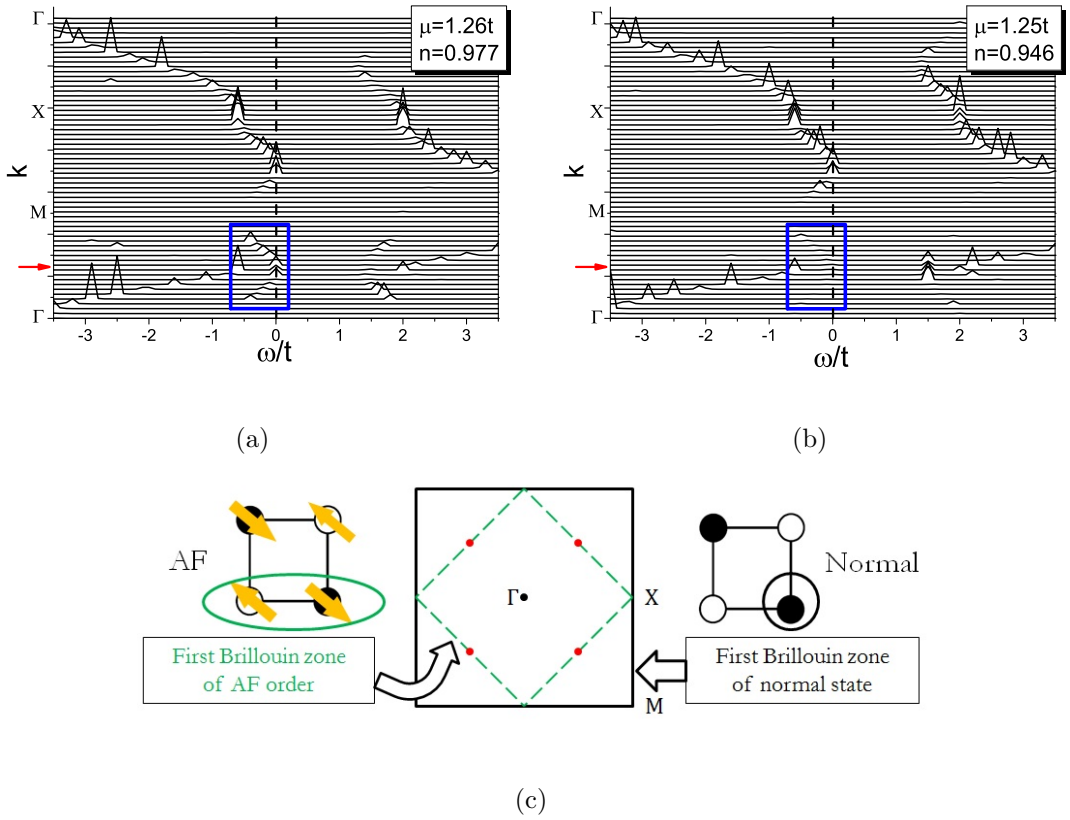

Fig. 6.4: One-particle excitation spectral functions for the Hubbard model on the square lattice right before and after phase separation are shown at (a) $\mu = 1.26$ ($n = 0.977$) (b) $\mu = 1.25$ ($n = 0.947$). The dotted line at $\omega = 0$ denotes the Fermi level. At the higher electron density ($n = 0.977$), a part of the spectra in (a), which is enclosed in the blue square, shows up around $(\pi/2, \pi/2)$ point (marked by red arrow) at the Fermi level, but it vanishes in (b) at the lower density $n = 0.947$ (almost no peaks in the blue square). (c) shows the first Brillouin zone (FBZ) of a square lattice and the k-points shown in (a) and (b) are also marked. The FBZs for the AF state and the normal state are different as shown in this figure.

The above analysis of the spectral function indicates that when the electronic phase separation happens, there is a Fermi surface instability caused by the deformation of the FBZ boundary. This observation leads us to believe that there could be some kind of causality between the electronic phase separation and the deformation of the FBZ boundary. One possible reason is that the deformation of the FBZ boundary leads to an instability of the Fermi surface and these offsets create a dramatic change in the free energy of the lattice which makes the chemical potential of these two different states the same. This process eventually leads to the electronic phase separation.

How to examine the above statement? One possible way is to study another lattice that does not have a deformation of the FBZ boundary and an instability of the Fermi surface. If this new lattice does not show any electronic phase separation, the instability of the Fermi surface caused by a deformation of the FBZ boundary would be one crucial reason for the electronic phase separation.

6.2.2 Studies of the honeycomb lattice

In order to examine the statement discussed in the previous section, we have carried out a study the Hubbard model on a honeycomb lattice. The reason to choose a honeycomb lattice is that the honeycomb lattice always has two sites per unit cell, no matter whether it is in an AF state or a metallic state, so when the honeycomb lattice undergoes a phase transition from an AF state to a

metallic state, there is no deformation of FBZ boundary (See Fig. 6.5(c)). The one-particle excitation spectral function extracted from VCA calculations of the Hubbard model on a honeycomb lattice confirms that there is no instability of the Fermi surface. The spectral function at $U = 4$ is shown in Fig. 6.5. The evolution of the spectrum shows a smooth transition of the Fermi level and the Fermi surface instability is not observed in the honeycomb lattice.

Absence of electronic phase separation in the honeycomb lattice

The n vs. μ plots for the honeycomb lattice are also smooth for all the U values and there is no sign of electronic phase separation instabilities. Although the Mott-Hubbard transition at half-filling for the honeycomb lattice occurs at a larger U_c, there are no indications of phase separation discontinuities in a similar region of hole doping before and after this transition. The only difference between our studies of the honeycomb lattice and the square lattice is the geometry of the lattice and both geometries are bipartite which means that they both have electron-hole symmetry. The distinct behaviors between the two types of lattices indicate that the geometry of lattice is important to electronic phase separation. A main reason for electronic phase separation is a geometry-caused deformation of the first Brillouin zone boundary.

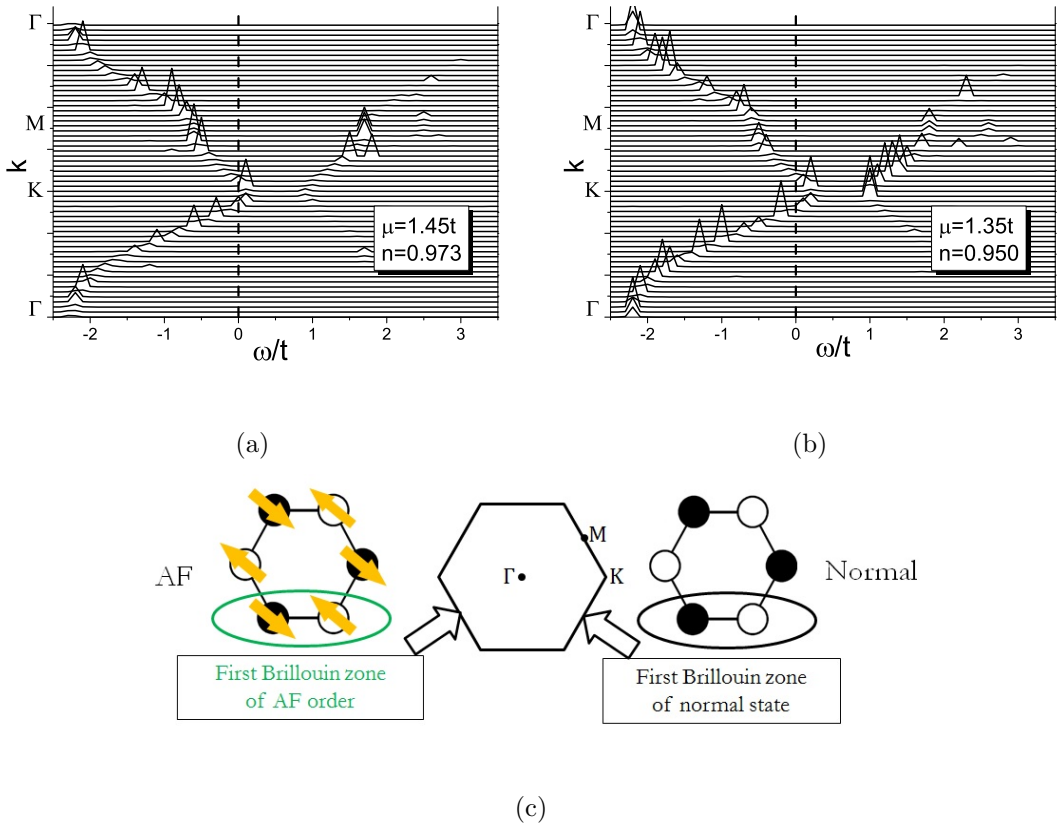

Fig. 6.5: One-particle excitation spectral functions for the Hubbard model on the honeycomb lattice with similar electron density with Fig. 6.4: (a) $\mu = 1.45$ ($n = 0.970$) (b) $\mu = 1.35$ ($n = 0.950$). The dotted line at $\omega = 0$ denotes the Fermi level. The spectra do not change too much between two electron densities. The missing spectrum observed in the square lattice (Fig. 6.4) is not found in the honeycomb lattice, which implies that there is no instability of the Fermi surface. (c) shows the first Brillouin zone (FBZ) of a honeycomb lattice and the k-points shown in (a) and (b) are also marked. The FBZs for the AF state and the normal state are the same for the honeycomb lattice.

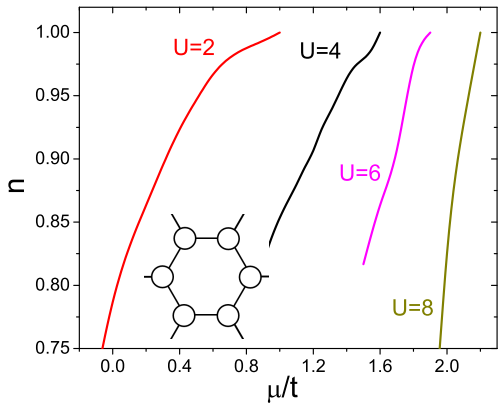

Fig. 6.6: The electron densities n as a function of chemical potential μ for the Hubbard model on a honeycomb lattice at different values of on-site Coulomb interaction U. The plots for the honeycomb lattice are smooth without any discontinuities which implies that phase separation is absent in the honeycomb lattice. The reference systems used in the VCA calculation are shown in the inset of corresponding plots.

6.3 Summary

In this chapter, We have studied possible electronic phase separation in the Hubbard model for the square and honeycomb lattices using the VCA method. The calculations in the square lattice provide strong support that electronic phase separation is a many-body effect and closely related to the AF transition. By studying the spectral function, we found that electronic phase separation might be a result of a Fermi surface instability which is the result of a geometry-related deformation of the FBZ boundary: when the square lattice transits from an AF state to a metallic state, the number of lattice sites per unit cell will change from 2 to 1 causing a deformation of the FBZ boundary. This is also confirmed by our study of the honeycomb lattice. Our VCA calculations also provide substantial support for the phase-separation tendency obtained at the isolated quantum cluster level in Chapter 3, *i.e.*, electronic phase separation observed in small square clusters persists in the larger systems.

Bibliography

[1] N.W. Ashcroft and N.D. Mermin. *Solid state physics*. Science: Physics. Saunders College, 1976.

[2] R.G. Parr and W. Yang. *Density-Functional Theory of Atoms and Molecules*. International Series of Monographs on Chemistry. Oxford University Press, USA, 1989.

[3] A.A. Abrikosov, L.P. Gorkov, I.E. Dzyaloshinski, and I.E. Dzialoshinskiĭ. *Methods of Quantum Field Theory in Statistical Physics*. Dover Books on Physics Series. Dover Publications, 1975.

[4] Elbio Dagotto. Complexity in Strongly Correlated Electronic Systems. *Science*, 309(5732):257–262, 2005.

[5] Andrea Damascelli, Zahid Hussain, and Zhi-Xun Shen. Angle-resolved photoemission studies of the cuprate superconductors. *Rev. Mod. Phys.*, 75:473–541, Apr 2003.

[6] J. Hubbard. Electron correlations in narrow energy bands. *Proceedings of the Royal Society of London. Series A. Mathematical and Physical Sciences*, 276(1365):238–257, 1963.

[7] Hirokazu Tsunetsugu, Manfred Sigrist, and Kazuo Ueda. The ground-state phase diagram of the one-dimensional Kondo lattice model. *Rev. Mod. Phys.*, 69:809–864, Jul 1997.

[8] P. W. Anderson. Localized Magnetic States in Metals. *Phys. Rev.*, 124:41–53, Oct 1961.

[9] S. H. Pan, J. P. O'Neal, R. L. Badzey, C. Chamon, H. Ding, J. R. Engelbrecht, Z. Wang, H. Eisaki, S. Uchida, A. K. Gupta, K.-W. Ng, E. W. Hudson, K. M. Lang, and J. C. Davis. Microscopic electronic inhomogeneity in the high-T_c superconductor $Bi_2Sr_2CaCu_2O_{8+x}$. *Nature*, 413:282–285, September 2001.

[10] M. C. Boyer, W. D. Wise, K. Chatterjee, M. Yi, T. Kondo, T. Takeuchi, H. Ikuta, and E. W. Hudson. Imaging the two gaps of the high-temperature superconductor $Bi_2Sr_2CuO_{6+x}$. *Nature Physics*, 3:802–806, November 2007.

[11] H. E. Mohottala, B. O. Wells, J. I. Budnick, W. A. Hines, C. Niedermayer, L. Udby, C. Bernhard, A. R. Moodenbaugh, and F.-C. Chou. Phase separation in superoxygenated $La_{2-x}Sr_xCuO_{4+y}$. *Nature Materials*, 5:377–382, May 2006.

[12] J. T. Park, D. S. Inosov, Ch. Niedermayer, G. L. Sun, D. Haug, N. B. Christensen, R. Dinnebier, A. V. Boris, A. J. Drew, L. Schulz, T. Shapoval, U. Wolff, V. Neu, Xiaoping Yang, C. T. Lin, B. Keimer, and V. Hinkov. Electronic Phase Separation in the Slightly Underdoped Iron Pnictide Superconductor $Ba_{1-x}K_xFe_2As_2$. *Phys. Rev. Lett.*, 102:117006, Mar 2009.

[13] E. D. Bauer, Yi-feng Yang, C. Capan, R. R. Urbano, C. F. Miclea, H. Sakai, F. Ronning, M. J. Graf, A. V. Balatsky, R. Movshovich, A. D. Bianchi, A. P. Reyes, P. L. Kuhns, J. D. Thompson, and Z. Fisk. Electronic inhomogeneity in a Kondo lattice. *Proceedings of the National Academy of Sciences*, 108(17):6857–6861, 2011.

[14] J. M. Tranquada, B. J. Sternlieb, J. D. Axe, Y. Nakamura, and S. Uchida. Evidence for stripe correlations of spins and holes in copper oxide superconductors. *Nature*, 375(6532):561–563, 1995.

[15] J. E. Hoffman, E. W. Hudson, K. M. Lang, V. Madhavan, H. Eisaki, S. Uchida, and J. C. Davis. A Four Unit Cell Periodic Pattern of Quasi-Particle States Surrounding Vortex Cores in $Bi_2Sr_2CaCu_2O_{8+}$. *Science*, 295(5554):466–469, 2002.

[16] K. M. Lang, V. Madhavan, J. E. Hoffman, E. W. Hudson, H. Eisaki, S. Uchida, and J. C. Davis. Imaging the granular structure of high-T_c superconductivity in underdoped $Bi_2Sr_2CaCu_2O_{8+\delta}$. *Nature*, 415:412–416, January 2002.

[17] V. Hinkov, D. Haug, B. Fauqu, P. Bourges, Y. Sidis, A. Ivanov, C. Bernhard, C. T. Lin, and B. Keimer. Electronic Liquid Crystal State in the High-Temperature Superconductor $YBa_2Cu_3O_{6.45}$. *Science*, 319(5863):597–600, 2008.

[18] M. J. Lawler, K. Fujita, J. Lee, A. R. Schmidt, Y. Kohsaka, C. K. Kim, H. Eisaki, S. Uchida, J. C. Davis, J. P. Sethna, and E.-A. Kim. Intra-unit-cell electronic nematicity of the high-T_c copper-oxide pseudogap states. *Nature*, 466:347–351, July 2010.

[19] J. M. Tranquada, H. Woo, T. G. Perring, H. Goka, G. D. Gu, G. Xu, M. Fujita, and K. Yamada. Quantum magnetic excitations from stripes in copper oxide superconductors. *Nature*, 429:534–538, June 2004.

[20] P. B. Visscher. Phase separation instability in the Hubbard model. *Phys. Rev. B*, 10:943–945, Aug 1974.

[21] V. J. Emery, S. A. Kivelson, and H. Q. Lin. Phase separation in the t - J model. *Phys. Rev. Lett.*, 64:475–478, Jan 1990.

[22] V.J. Emery and S.A. Kivelson. Frustrated electronic phase separation and high-temperature superconductors. *Physica C: Superconductivity*, 209(4):597–621, May 1993.

[23] Gang Su. Phase separation in the two-dimensional Hubbard model. *Phys. Rev. B*, 54:R8281–R8284, Sep 1996.

[24] Armen N. Kocharian, Gayanath W. Fernando, Kalum Palandage, and James W. Davenport. Exact study of charge-spin separation, pairing fluctuations, and pseudogaps in four-site Hubbard clusters. *Phys. Rev. B*, 74:024511, Jul 2006.

[25] G. W. Fernando, A. N. Kocharian, K. Palandage, Tun Wang, and J. W. Davenport. Phase separation and electron pairing in repulsive Hubbard clusters. *Phys. Rev. B*, 75:085109, Feb 2007.

[26] A. N. Kocharian, G. W. Fernando, K. Palandage, and J. W. Davenport. Coherent and incoherent pairing instabilities and spin-charge separation in bipartite and nonbipartite nanoclusters: Exact results. *Phys. Rev. B*, 78:075431, Aug 2008.

[27] G. W. Fernando, K. Palandage, A. N. Kocharian, and J. W. Davenport. Pairing in bipartite and nonbipartite repulsive Hubbard clusters: Octahedron. *Phys. Rev. B*, 80:014525, Jul 2009.

[28] Kun Fang, G. W. Fernando, and A. N. Kocharian. Pairing enhancement in Betts lattices with next nearest neighbor couplings: Exact results. *Physics Letters A*, 376(4):538 – 543, 2012.

[29] A. Macridin, M. Jarrell, and Th. Maier. Phase separation in the Hubbard model using the dynamical cluster approximation. *Phys. Rev. B*, 74:085104, Aug 2006.

[30] E. Khatami, K. Mikelsons, D. Galanakis, A. Macridin, J. Moreno, R. T. Scalettar, and M. Jarrell. Quantum criticality due to incipient phase separation in the two-dimensional Hubbard model. *Phys. Rev. B*, 81:201101, May 2010.

[31] M. Aichhorn, E. Arrigoni, M. Potthoff, and W. Hanke. Variational cluster approach to the Hubbard model: Phase-separation tendency and finite-size effects. *Phys. Rev. B*, 74:235117, Dec 2006.

[32] M. Aichhorn, E. Arrigoni, M. Potthoff, and W. Hanke. Phase separation and competition of superconductivity and magnetism in the two-dimensional Hubbard model: From strong to weak coupling. *Phys. Rev. B*, 76:224509, Dec 2007.

[33] A. O. Sboychakov, A. V. Rozhkov, A. L. Rakhmanov, and Franco Nori. Antiferromagnetic states and phase separation in doped AA-stacked graphene bilayers. *Phys. Rev. B*, 88:045409, Jul 2013.

[34] A. O. Sboychakov, A. V. Rozhkov, K. I. Kugel, A. L. Rakhmanov, and Franco Nori. Electronic phase separation in iron pnictides. *Phys. Rev. B*, 88:195142, Nov 2013.

[35] Elliott H. Lieb and F. Y. Wu. Absence of Mott Transition in an Exact Solution of the Short-Range, One-Band Model in One Dimension. *Phys. Rev. Lett.*, 20:1445–1448, Jun 1968.

[36] J. Als-Nielsen and R. J. Birgeneau. Mean field theory, the Ginzburg criterion, and marginal dimensionality of phase transitions. *American Journal of Physics*, 45(6):554–560, 1977.

[37] Antoine Georges, Gabriel Kotliar, Werner Krauth, and Marcelo J. Rozenberg. Dynamical mean-field theory of strongly correlated fermion systems and the limit of infinite dimensions. *Rev. Mod. Phys.*, 68:13–125, Jan 1996.

[38] D. Sénéchal, D. Perez, and M. Pioro-Ladrière. Spectral Weight of the Hubbard Model through Cluster Perturbation Theory. *Phys. Rev. Lett.*, 84:522–525, Jan 2000.

[39] Gabriel Kotliar, Sergej Y. Savrasov, Gunnar Pálsson, and Giulio Biroli. Cellular Dynamical Mean Field Approach to Strongly Correlated Systems. *Phys. Rev. Lett.*, 87:186401, Oct 2001.

[40] M. H. Hettler, A. N. Tahvildar-Zadeh, M. Jarrell, T. Pruschke, and H. R. Krishnamurthy. Nonlocal dynamical correlations of strongly interacting electron systems. *Phys. Rev. B*, 58:R7475–R7479, Sep 1998.

[41] M. Potthoff, M. Aichhorn, and C. Dahnken. Variational Cluster Approach to Correlated Electron Systems in Low Dimensions. *Phys. Rev. Lett.*, 91:206402, Nov 2003.

[42] W.H. Press. *Numerical Recipes in FORTRAN: The Art of Scientific Computing*. Number v. 1 in Fortran Numerical Recipes: The Art of Scientific Computing. Numerical Recipes in Fortran 77. Cambridge University Press, 1992.

[43] J.K. Cullum and R.A. Willoughby. *Lanczos Algorithms for Large Symmetric Eigenvalue Computations: Volume 1, Theory*. Classics in Applied Mathematics. Society for Industrial and Applied Mathematics, 2002.

[44] M. Potthoff. Self-energy-functional approach to systems of correlated electrons. *The European Physical Journal B - Condensed Matter and Complex Systems*, 32(4):429–436, 2003.

[45] Thomas Maier, Mark Jarrell, Thomas Pruschke, and Matthias H. Hettler. Quantum cluster theories. *Rev. Mod. Phys.*, 77:1027–1080, Oct 2005.

[46] C. Dahnken, M. Aichhorn, W. Hanke, E. Arrigoni, and M. Potthoff. Variational cluster approach to spontaneous symmetry breaking: The itinerant antiferromagnet in two dimensions. *Phys. Rev. B*, 70:245110, Dec 2004.

[47] David Sénéchal, P.-L. Lavertu, M.-A. Marois, and A.-M. S. Tremblay. Competition between Antiferromagnetism and Superconductivity in High-T_c Cuprates. *Phys. Rev. Lett.*, 94:156404, Apr 2005.

[48] M. Aichhorn, E. Arrigoni, M. Potthoff, and W. Hanke. Antiferromagnetic to superconducting phase transition in the hole- and electron-doped Hubbard model at zero temperature. *Phys. Rev. B*, 74:024508, Jul 2006.

[49] E.W. Carlson, V.J. Emery, S.A. Kivelson, and D. Orgad. Concepts in high temperature superconductivity. In K.H. Bennemann and JohnB. Ketterson, editors, *Superconductivity*, pages 1225–1348. Springer Berlin Heidelberg, 2008.

[50] A.N. Kocharian, G.W. Fernando, K. Palandage, and J.W. Davenport. Thermodynamic properties, magnetism and MottHubbard-like transitions in nanoscale clusters . *Journal of Magnetism and Magnetic Materials*, 300(1):e585 – e590, 2006.

[51] Wei-Feng Tsai and Steven A. Kivelson. Superconductivity in inhomogeneous Hubbard models. *Phys. Rev. B*, 73:214510, Jun 2006.

[52] D. D. Betts, S. Masui, N. Vats, and G. E. Stewart. Improved finite-lattice method for estimating the zero-temperature properties of two-dimensional lattice models. *Canadian Journal of Physics*, 74(1-2):54–64, 1996.

[53] D D Betts, H Q Lin, and J S Flynn. Improved finite-lattice estimates of the properties of two quantum spin models on the infinite square lattice. *Canadian Journal of Physics*, 77(5):353–369, 1999.

[54] J. Oitmaa and D. D. Betts. The ground state of two quantum models of magnetism. *Canadian Journal of Physics*, 56(7):897–901, 1978.

[55] J. E. Hirsch. Two-dimensional Hubbard model: Numerical simulation study. *Phys. Rev. B*, 31:4403–4419, Apr 1985.

[56] Elbio Dagotto. Correlated electrons in high-temperature superconductors. *Rev. Mod. Phys.*, 66:763–840, Jul 1994.

[57] S. A. Kivelson and E. Fradkin. How optimal inhomogeneity produces high temperature superconductivity. *eprint arXiv:cond-mat/0507459*, July 2005.

[58] Wei-Feng Tsai, Hong Yao, Andreas Läuchli, and Steven A. Kivelson. Optimal inhomogeneity for superconductivity: Finite-size studies. *Phys. Rev. B*, 77:214502, Jun 2008.

[59] A.N. Kocharian, G.W. Fernando, K. Palandage, and J.W. Davenport. Electron coherent and incoherent pairing instabilities in inhomogeneous bipartite and nonbipartite nanoclusters ". ,*Physics Letters A*, 373(11):1074 – 1082, 2009.

[60] A.N. Kocharian, G.W. Fernando, T. Wang, K. Palandage, and J.W. Davenport. Exact thermodynamics of pairing and chargespin separation crossovers in small Hubbard nanoclusters . *Physics Letters A*, 364(1):57 – 65, 2007.

[61] Wei-Feng Tsai, Hong Yao, Andreas Läuchli, and Steven A. Kivelson. Optimal inhomogeneity for superconductivity: Finite-size studies. *Phys. Rev. B*, 77:214502, Jun 2008.

[62] Daniel Duffy and Adriana Moreo. Influence of next-nearest-neighbor electron hopping on the static and dynamical properties of the two-dimensional Hubbard model. *Phys. Rev. B*, 52:15607–15616, Dec 1995.

[63] Steven R. White and D. J. Scalapino. Competition between stripes and pairing in a $t - t' - J$ model. *Phys. Rev. B*, 60:R753–R756, Jul 1999.

[64] G. Polatsek and K. W. Becker. Ground-state energy of the Hubbard model at half filling. *Phys. Rev. B*, 54:1637–1644, Jul 1996.

[65] H. Eisaki, N. Kaneko, D. L. Feng, A. Damascelli, P. K. Mang, K. M. Shen, Z.-X. Shen, and M. Greven. Effect of chemical inhomogeneity in bismuth-based copper oxide superconductors. *Phys. Rev. B*, 69:064512, Feb 2004.

[66] J.G. Bednorz and K.A. Mller. Possible high Tc superconductivity in the BaLaCuO system. *Zeitschrift fr Physik B Condensed Matter*, 64(2):189–193, 1986.

[67] C. W. Chu, L. Gao, F. Chen, Z. J. Huang, R. L. Meng, and Y. Y. Xue. Superconductivity above 150 K in $HgBa_2Ca_2Cu_3O_{8+\delta}$ at high pressures. *Nature*, 365:323–325, September 1993.

[68] J. A. Slezak, Jinho Lee, M. Wang, K. McElroy, K. Fujita, B. M. Andersen, P. J. Hirschfeld, H. Eisaki, S. Uchida, and J. C. Davis. Imaging the impact on cuprate superconductivity of varying the interatomic distances within individual crystal unit cells. *Proceedings of the National Academy of Sciences*, 105(9):3203–3208, 2008.

[69] Jinho Lee, K. Fujita, K. McElroy, J. A. Slezak, M. Wang, Y. Aiura, H. Bando, M. Ishikado, T. Masui, J.-X. Zhu, A. V. Balatsky, H. Eisaki, S. Uchida, and J. C. Davis. Interplay of electronlattice interactions and superconductivity in $Bi_2Sr_2CaCu_2O_{8+\delta}$. *Nature*, 442(7102):546–550, 2006.

[70] X. B. Kan and S. C. Moss. Four-dimensional crystallographic analysis of the incommensurate modulation in a $Bi_2Sr_2CaCu_2O_8$ single crystal. *Acta Crystallographica Section B*, 48(2):122–134, Apr 1992.

[71] Tamara S. Nunner, Brian M. Andersen, Ashot Melikyan, and P. J. Hirschfeld. Dopant-Modulated Pair Interaction in Cuprate Superconductors. *Phys. Rev. Lett.*, 95:177003, Oct 2005.

[72] P. W. ANDERSON. The Resonating Valence Bond State in La_2CuO_4 and Superconductivity. *Science*, 235(4793):1196–1198, 1987.

[73] Kai-Yu Yang, T. M. Rice, and Fu-Chun Zhang. Effect of superlattice modulation of electronic parameters on the density of states of cuprate superconductors. *Phys. Rev. B*, 76:100501, Sep 2007.

[74] Y. He, S. Graser, P. J. Hirschfeld, and H.-P. Cheng. Supermodulation in the atomic structure of the superconductor $Bi_2Sr_2CaCu_2O_{8+x}$ from *ab initio* calculations. *Phys. Rev. B*, 77:220507, Jun 2008.

[75] Tadashi Machida, Takuya Kato, Hiroshi Nakamura, Masaki Fujimoto, Takashi Mochiku, Shuuichi Ooi, Ajay D. Thakur, Hideaki Sakata, and Kazuto Hirata. Quantum interference of impurity bound states in

$Bi_2Sr_2Ca(Cu_{1-x}Zn_x)_2O_{8+\delta}$ probed by scanning tunneling spectroscopy. *Phys. Rev. B*, 84:064501, Aug 2011.

[76] J. González. *Quantum Electron Liquids and High-Tc Superconductivity*. Number v. 38 in Ernst Schering Research Foundation Workshops. Springer, 1995.

[77] A. K. McMahan, Richard M. Martin, and S. Satpathy. Calculated effective Hamiltonian for La_2CuO_4 and solution in the impurity Anderson approximation. *Phys. Rev. B*, 38:6650–6666, Oct 1988.

[78] D. M. Newns, P. C. Pattnaik, and C. C. Tsuei. Role of Van Hove singularity in high-temperature superconductors: Mean field. *Phys. Rev. B*, 43:3075–3084, Feb 1991.

[79] I. Zeljkovic, Z. Xu, J. Wen, G. Gu, R. S. Markiewicz, and J. E. Hoffman. Imaging the Impact of Single Oxygen Atoms on Superconducting $Bi_{2+y}Sr_{2-y}CaCu_2O_{8+x}$. *Science*, 337:320–, July 2012.

[80] A. Bianconi, M. Lusignoli, N. L. Saini, P. Bordet, Å. Kvick, and P. G. Radaelli. Stripe structure of the CuO_2 plane in $Bi_2Sr_2CaCu_2O_{8+y}$ by anomalous x-ray diffraction. *Phys. Rev. B*, 54:4310–4314, Aug 1996.

[81] D. Sénéchal. An introduction to quantum cluster methods. *ArXiv e-prints*, June 2008.

[82] R. A. Borzi, S. A. Grigera, J. Farrell, R. S. Perry, S. J. S. Lister, S. L. Lee, D. A. Tennant, Y. Maeno, and A. P. Mackenzie. Formation of a Nematic Fluid at High Fields in $Sr_3Ru_2O_7$. *Science*, 315(5809):214–217, 2007.

[83] L. W. Harriger, H. Q. Luo, M. S. Liu, C. Frost, J. P. Hu, M. R. Norman, and Pengcheng Dai. Nematic spin fluid in the tetragonal phase of $BaFe_2As_2$. *Phys. Rev. B*, 84:054544, Aug 2011.

[84] Jiun-Haw Chu, James G. Analytis, Kristiaan De Greve, Peter L. McMahon, Zahirul Islam, Yoshihisa Yamamoto, and Ian R. Fisher. In-Plane Resistivity Anisotropy in an Underdoped Iron Arsenide Superconductor. *Science*, 329(5993):824–826, 2010.

[85] Yoichi Ando, Kouji Segawa, Seiki Komiya, and A. N. Lavrov. Electrical Resistivity Anisotropy from Self-Organized One Dimensionality in High-Temperature Superconductors. *Phys. Rev. Lett.*, 88:137005, Mar 2002.

[86] M. A. Tanatar, E. C. Blomberg, A. Kreyssig, M. G. Kim, N. Ni, A. Thaler, S. L. Bud'ko, P. C. Canfield, A. I. Goldman, I. I. Mazin, and R. Prozorov.

Uniaxial-strain mechanical detwinning of $CaFe_2As_2$ and $BaFe_2As_2$ crystals: Optical and transport study. *Phys. Rev. B*, 81:184508, May 2010.

[87] R. Daou, J. Chang, David LeBoeuf, Olivier Cyr-Choinire, Francis Lalibert, Nicolas Doiron-Leyraud, B. J. Ramshaw, Ruixing Liang, D. A. Bonn, W. N. Hardy, and Louis Taillefer. Broken rotational symmetry in the pseudogap phase of a high-Tc superconductor. *Nature*, 463(7280):519–522, 2010.

[88] Eduardo Fradkin, Steven A. Kivelson, Michael J. Lawler, James P. Eisenstein, and Andrew P. Mackenzie. Nematic Fermi Fluids in Condensed Matter Physics. *Annual Review of Condensed Matter Physics*, 1(1):153–178, 2010.

[89] S. Okamoto, D. Sénéchal, M. Civelli, and A.-M. S. Tremblay. Dynamical electronic nematicity from Mott physics. *Phys. Rev. B*, 82:180511, Nov 2010.

[90] A.N. Kocharian, Kun Fang, and G.W. Fernando. Exact quantum critical points and phase separation instabilities in Betts Hubbard nanoclusters . *Journal of Magnetism and Magnetic Materials*, 324(21):3427 – 3431, 2012. Fifth Moscow international symposium on magnetism.

[91] R S Markiewicz. Phase separation near the Mott transition in $La_{2-x}Sr_xCuO_4$. *Journal of Physics: Condensed Matter*, 2(3):665, 1990.

[92] M. Capone, G. Sangiovanni, C. Castellani, C. Di Castro, and M. Grilli. Phase Separation Close to the Density-Driven Mott Transition in the Hubbard-Holstein Model. *Phys. Rev. Lett.*, 92:106401, Mar 2004.

[93] B. V. Fine and T. Egami. Phase separation in the vicinity of quantum-critical doping concentration: Implications for high-temperature superconductors. *Phys. Rev. B*, 77:014519, Jan 2008.

[94] Y. Z. Zhang and Masatoshi Imada. Pseudogap and Mott transition studied by cellular dynamical mean-field theory. *Phys. Rev. B*, 76:045108, Jul 2007.

[95] M. Balzer, B. Kyung, D. Snchal, A.-M. S. Tremblay, and M. Potthoff. First-order Mott transition at zero temperature in two dimensions: Variational plaquette study. *EPL (Europhysics Letters)*, 85(1):17002, 2009.

[96] M. Vekić and S. R. White. Pseudogap formation in the half-filled Hubbard model. *Phys. Rev. B*, 47:1160–1163, Jan 1993.

[97] S. Sorella and E. Tosatti. Semi-Metal-Insulator Transition of the Hubbard Model in the Honeycomb Lattice. *EPL (Europhysics Letters)*, 19(8):699, 1992.

[98] Minh-Tien Tran and Kazuhiko Kuroki. Finite-temperature semimetal-insulator transition on the honeycomb lattice. *Phys. Rev. B*, 79:125125, Mar 2009.

[99] G. Santoro, M. Airoldi, S. Sorella, and E. Tosatti. Hubbard model on the infinite-dimensional diamond lattice. *Phys. Rev. B*, 47:16216–16221, Jun 1993.

[100] L.D. Landau and E.M. Lifshitz. *Statistical Physics*, volume 5. Elsevier Science, 1996.

[101] Nobuo Furukawa, T. M. Rice, and Manfred Salmhofer. Truncation of a Two-Dimensional Fermi Surface due to Quasiparticle Gap Formation at the Saddle Points. *Phys. Rev. Lett.*, 81:3195–3198, Oct 1998.

[102] N Furukawa and T M Rice. Instability of a Landau - Fermi liquid as the Mott insulator is approached. *Journal of Physics: Condensed Matter*, 10(23):L381, 1998.